

Clemson University

TigerPrints

All Theses

Theses

5-2024

Layered Structure Protonic Ceramic Conductors of the Form $Ba_5In_{2+x}Al_2Zr_{1-x}O_{13-\delta}$

Nathan Cretegny
ncreteg@clemson.edu

Follow this and additional works at: https://tigerprints.clemson.edu/all_theses



Part of the [Ceramic Materials Commons](#)

Recommended Citation

Cretegny, Nathan, "Layered Structure Protonic Ceramic Conductors of the Form $Ba_5In_{2+x}Al_2Zr_{1-x}O_{13-\delta}$ " (2024). *All Theses*. 4273.

https://tigerprints.clemson.edu/all_theses/4273

This Thesis is brought to you for free and open access by the Theses at TigerPrints. It has been accepted for inclusion in All Theses by an authorized administrator of TigerPrints. For more information, please contact kokeefe@clemson.edu.

**LAYERED STRUCTURE PROTONIC CERAMIC
CONDUCTORS OF THE FORM $Ba_5In_{2+x}Al_2Zr_{1-x}O_{13-\delta}$**

A Thesis
Presented to
the Graduate School of
Clemson University

In partial Fulfillment
of the Requirements for the Degree
Master of Science
Material Science and Engineering

by
Nathan Creteigny
May 2024

Accepted by:
Dr. Kyle S. Brinkman, Committee Chair
Dr. Pedro B. Groszewicz
Dr. Jianhua Tong
Dr. Mark A. Johnson

ABSTRACT

Layered perovskites have been studied as proton conductors throughout the past decade, with growing interest in layered hexagonal perovskites. The P63/mmc hexagonal perovskite space group is a class of intrinsically oxygen deficient layered perovskites showing exceptional proton conductivity, exhibiting total conductivities above 10^{-4} S cm⁻¹ at 600°C in wet air. These materials are ideal for applications in protonic ceramic fuel cells, which can operate at lower temperatures than conventional solid oxide fuel cells.

In this work, the hexagonal perovskite of targeted composition Ba₅In_{2+x}Al₂Zr_{1-x}O₁₃ (x=0, 0.1, 0.2) was synthesized via a solid-state synthesis route to study the impact of oxygen vacancy concentration in layered hexagonal perovskites. Precursor oxides were mixed in stoichiometric proportions, calcined between 800-1200°C and sintered at 1475°C. The sintered pellets were crushed into fine powders to investigate the chemistry and structure through X-ray diffraction, neutron diffraction, inductively coupled plasma mass spectrometry, and nuclear magnetic resonance. Dense pellets were used to study conductivity properties using electrochemical impedance spectroscopy.

The synthesis approach produced 100% phase pure material across a range of increasing indium content from 2.0 to 2.8, although not of the projected stoichiometries. Neutron diffraction and x-ray diffraction indicated fractional occupancy and site swapping of the indium and aluminum positions, which was not dependent on indium content and resulted in the newly detected O5 position.

From nuclear magnetic resonance, aluminum was proven to retain a strictly tetrahedral coordination. This provided strong evidence of one-way site swapping, with octahedral indium

having a 20% statistical occupancy of the aluminum position in the hexagonal layer.

Additionally, the existence of four bulk protons was observed. Three proton signals were a result of hydration, while the fourth site remained in the crystal structure after dehydration. Eight distinct oxygen signals were detected, although only the O2 signal was identified.

Impedance spectroscopy indicated a reduction of total conductivity at 600°C from 10^{-4} to 10^{-5} S cm⁻¹ from wet to dry air, with proton conduction consistent across the temperature range. Tests from all environments were unable to separate bulk from grain boundary conductivity.

ACKNOWLEDGEMENTS

I want to thank the many people at Clemson University and TUDelft who've helped me complete my research. First and foremost, thank you to my advisor Dr. Kyle S. Brinkman for the opportunities, guidance, and encouragement offered over the past two years. A massive thank you to Dr. Pedro B. Groszewicz, who taught me everything I know about NMR and made my experience at TUDelft something I'll never forget. Thank you to Dr. Mark Johnson and Dr. Jinhua Tong for your advice on my future and participation on my defense committee. To Dr. Marek Urban, thank you for providing the opportunity to conduct research at TUDelft during my Master's studies.

To the students and faculty who've helped me achieve this work, thank you for your encouragement and support. I could not have done it all without my group members Joshua Willoughby, Rahul Rajeev, Nakeshma Cassel, and Dr. Abhaya Mishra, who I could always count on when I needed to. Thank you to Dr. Jack Duffy for your mentorship during my first year in the group as an undergraduate, I would not have found my passion for research without your insight. To Abdulkadir Biffo overseas, thank you for your commitment to this project and thorough analysis of my work. I'd like to extend my appreciation to everyone in the MSE department, at AMRL, and at Savannah River National Lab who helped me accomplish so much in a short time frame.

Lastly, I'd like to thank my family for their unwavering support of my studies. Thank you Mom for all the phone calls of encouragement, thank you Papa for your personal and material science advice, and thank you Damien for being an outlet when I needed a break from the world.

TABLE OF CONTENTS

ABSTRACT.....	2
ACKNOWLEDGEMENTS.....	4
LIST OF FIGURES	7
LIST OF TABLES	8
NOMENCLATURE AND ABBREVIATION	9
CHAPTER 1. INTRODUCTION.....	10
1.1 Background Information.....	10
1.2 Experimental Methods.....	13
1.2.1 Solid-state Nuclear Magnetic Resonance (ss-NMR).....	13
1.2.2 Heteronuclear Correlation (HETCOR).....	14
1.2.3 Transfer of Populations in Double Resonance (TRAPDOR)	15
1.2.4 Multiple quantum magic angle spinning (MQMAS).....	16
1.2.5 Electrochemical Impedance Spectroscopy (EIS).....	17
CHAPTER 2. BIAZ SYNTHESIS, CHEMISTRY, AND CRYSTAL STRUCTURE.....	20
2.1 Synthesis of BIAZ.....	20
2.2 Chemistry of BIAZ	20
2.3 Crystal Structure of BIAZ.....	22
2.3.1 XRD of BIAZ	23
2.3.2 NPD of BIAZ.....	25
2.4 Analysis of BIAZ structure and chemistry.....	27
CHAPTER 3. NMR ANALYSIS OF BIAZ.....	32
3.1 Preparation of NMR samples and experimental conditions	32
3.2 ^1H NMR	33
3.3 ^{27}Al NMR.....	37
3.4 2D ^1H - ^{27}Al NMR	38
3.4.1 ^1H - ^{27}Al HETCOR NMR	38
3.4.2 ^1H - ^{27}Al TRAPDOR NMR.....	40
3.5 ^{17}O 1D and ^{17}O 3QMAS NMR.....	42
3.5.1 1D ^{17}O NMR.....	42
3.5.2 3QMAS ^{17}O NMR	43
3.6 Discussion of NMR results	45

3.6.1 ^1H NMR	45
3.6.2 ^{27}Al NMR.....	51
3.6.3 ^{17}O NMR.....	51
CHAPTER 4. EIS ANALYSIS OF BIAZ.....	53
4.1 Preparation of EIS samples and experimental conditions.....	53
4.2 Wet air EIS of BIAZ	53
4.3 Dry air EIS of BIAZ	55
4.6 Analysis of EIS results	58
4.6.1 Proton behavior in BIAZ	58
4.6.2 Activation energy of BIAZ	61
4.6.3 BIAZ conductivity in context	63
CHAPTER 5. CONCLUSIONS AND FUTURE WORK	65
5.1 Chemistry and structure of BIAZ	65
5.2 Conductivity of BIAZ.....	66
5.3 Future Work	66
REFERENCES	68

LIST OF FIGURES

Figure 1. Simple model of PCFC.....	11
Figure 2. Comparison of BEAZ with other proton conductors. BaZr _{0.8} Y _{0.2} O _{2.9} (BZO), BaCe _{0.9} Y _{0.1} O _{2.95} (BCO), BaIn _{1.6} Ti _{0.4} O _{5.2} (BITO), Ba ₃ Ca _{1.18} Nb _{1.82} O _{8.73} (BCN), La _{0.8} Ba _{1.2} GaO _{3.9} (LBGO), La _{0.99} Ca _{0.01} NbO _{3.995} (LNO), La ₂₆ O ₂₇ (BO ₃) (LBO), La _{5.4} MoO _{11.1} (LMO), La _{0.9} Sr _{0.1} PO _{3.95} (LPO). Figure taken with permission from High Proton Conductivity in Ba ₅ Er ₂ Al ₂ ZrO ₁₃ , a Hexagonal Perovskite Related Oxide with Intrinsically Oxygen-Deficient Layers (Murakami et al.) ⁵	12
Figure 3. Representation of the permanent magnetic field B ₀ (orange) and a sample's nuclear magnetic dipole (blue) in an NMR sequence. The dipole begins aligned with B ₀ , followed by a radiofrequency pulse rotating the dipole, which then realigns itself to the permanent magnetic field. ^{12,13}	14
Figure 4. Example of ¹ H- ²⁷ Al TRAPDOR experiment, with the respective nuclear irradiation patterns and NMR spectra ¹⁷	16
Figure 5. Unit cell of BIAZ from a) polyhedral perspective and b) atom/bond perspective. Barium, indium, aluminum, zirconium, and oxygen are red, pink, purple, blue, and white/gray, respectively. Images created using VESTA software, structural model created from Shpanchenko et al XRD refinement ⁶	22
Figure 6. Diffractogram of varying BIAZ compositions and the BIAZ reference ⁶	23
Figure 7. XRD refinement revealing statistical occupancy of the aluminum position (z = 0.397). Black bar represents indium occupancy, red represents aluminum occupancy. Samples defined by their projected stoichiometries.....	24
Figure 8. NPD diffractogram of BIAZ _{2.0}	25
Figure 9. Refined BIAZ model based upon NPD and XRD results. Model produced in VESTA. Barium, indium, aluminum, zirconium, and oxygen are red, pink, purple, blue, and white/gray, respectively, with the O5 site highlighted in black.....	26
Figure 10. c-axis lattice constant of BIAZ with varying indium content.....	28
Figure 11. ab lattice constant of BIAZ with varying indium content.....	28
Figure 12. Majority and minority crystal structures of BIAZ based upon refinement. Full occupancy of atomic sites is used for clarity. Left) Majority structure BIAZ with a single O3 site in the h' layer coordinated by aluminum. Right) Minority structure BIAZ with three O5 sites in the h' layer coordinated by indium. Barium, indium, aluminum, zirconium, and oxygen are red, pink, purple, blue, and white/gray, respectively. Models made using VESTA software.	30
Figure 13. ¹ H NMR fitted spectrum of hydrated BIAZ _{2.6} (MAS 22kHz).....	34
Figure 14. ¹ H NMR of BIAZ _{2.6} with varying sample preparations (MAS 22kHz). Red, blue, and purple, are ¹⁷ O enriched, hydrated, and ¹⁷ O enriched + hydrated, respectively.....	35
Figure 15. ²⁷ Al NMR of BIAZ _{2.6} (MAS 18kHz), 6.2 ppm peak indicated by arrow.....	37
Figure 16. ¹ H- ²⁷ Al HETCOR NMR of hydrated BIAZ _{2.6}	39
Figure 17. ¹ H- ²⁷ Al HETCOR NMR of ¹⁷ O enriched BIAZ _{2.0}	40
Figure 18. Example of attainable ¹ H- ²⁷ Al TRAPDOR fraction of BIAZ.....	41
Figure 19. Example of unattainable ¹ H- ²⁷ Al TRAPDOR fraction of BIAZ.....	41

Figure 20. 1D ^{17}O NMR of ^{17}O enriched BIAZ2.6 (MAS 22kHz). Black arrow points out real 233 ppm ^{17}O signal.	43
Figure 21. ^{17}O 3QMAS NMR of BIAZ2.6 (MAS 22kHz)	44
Figure 22. Crystal structure of BIAZ highlighting NMR investigated nuclear positions. Protons are shown at predicted sites identified via ^1H NMR, size and quantity of protons are not to scale.	47
Figure 23. Minority crystal structure BIAZ, with O5 occupying the h' layer rather than O3. Protons are shown at predicted sites identified via ^1H NMR, size and quantity of protons are not to scale.	48
Figure 24. Nyquist plot of BIAZ2.6 from 400°C to 500°C in wet air conditions with associated equivalent circuit.....	54
Figure 25. Conductivity trends of BIAZ in wet air conditions	55
Figure 26. Nyquist plot of BIAZ2.6 in dry air conditions with associated equivalent circuit.....	56
Figure 27. Conductivity trends of BIAZ in dry air conditions	57
Figure 28. Estimated proton conductivity of BIAZ from wet and dry air conditions	58
Figure 29. Estimated proton transport number of BIAZ from wet and dry air conditions	60

LIST OF TABLES

Table 1. ICP-MS results of BIAZ samples, normalized to expected aluminum content	21
Table 2. Lattice parameters of hexagonal perovskite BIAZ	24
Table 3. Experimental matrix of NMR samples	33
Table 4. ^1H NMR summary of BIAZ.....	36
Table 5. ^{27}Al NMR parameters of BIAZ.....	38
Table 6. ^1H - ^{27}Al TRAPDOR fractions of proton signals in BIAZ.....	42
Table 7. Summary of ^{17}O signals detected in BIAZ	44
Table 8. Previous literature analysis of NMR data obtained from similar materials	50
Table 9. Activation energies of BIAZ from 550°C to 650°C (units of eV).....	62
Table 10. Activation energies of BIAZ from 400°C to 450°C (units of eV).....	63

NOMENCLATURE AND ABBREVIATION

Abbreviation	Meaning
BIAZ	The general material $Ba_5In_2Al_2ZrO_{13-\delta}$, with exact stoichiometry unspecified
BIAZ2.0, BIAZ2.6, BIAZ2.8	Prepared samples of $Ba_yIn_{2+x}Al_2Zr_zO_{13}$, where the acronym indicates BIAZ2.X
BEAZ	$Ba_5Er_2Al_2ZrO_{13-\delta}$
XRD	X-ray diffraction
NPD	Neutron powder diffraction
ICPMS	Inductively coupled plasma mass spectrometry
NMR	Nuclear magnetic resonance
HETCOR	Heteronuclear correlation
TRAPDOR	Transfer of populations in double resonance
MQMAS	Multiple quantum magic angle spinning
EIS	Electrochemical impedance spectroscopy
σ_{wet}	Total conductivity in wet air
σ_{dry}	Total conductivity in dry air
σ_{H^+}	Conductivity of protons
t_{H^+}	Transport number of protons

CHAPTER 1. INTRODUCTION

1.1 Background Information

Given the global concern of climate change, research and development of sustainable energy technologies has become increasingly necessary. Fuel cells use chemical energy to generate electricity, allowing for more efficient energy generation relative to internal combustion engines¹. Traditional solid oxide fuel cells (SOFCs) operate by oxidizing fuel at the anode and reducing oxygen at cathode, allowing for electrons to travel through an external circuit while oxygen ions are conducting through the electrolyte produce waste products at the anode. Protonic ceramic fuel cells (PCFCs) operate in a nearly identical fashion, the key difference being proton conduction across the electrolyte rather than oxygen ions, which results in waste products being formed at the cathode rather than the anode^{2,3}. Ideally, pure hydrogen is used as the fuel, resulting in strictly water waste and an energy technology free of greenhouse gas emissions.

A key goal in the development of fuel cells is reducing operating temperatures while maintaining or improving ionic/protonic conduction. High temperature fuel cells run at 700 - 1000°C, but lowering the temperature is crucial for minimizing material degradation, reducing operating costs, and reducing start-up times^{2,4}, causing a shift towards PCFCs in recent years due to their lower temperature capabilities³. In 2020, Murakami et al. discovered the hexagonal perovskite $\text{Ba}_5\text{Er}_2\text{Al}_2\text{ZrO}_{13}$ (BEAZ) was capable of incorporating protons into the oxygen-deficient layer, exhibiting proton conductivity around $5 \cdot 10^{-3} \text{ S cm}^{-1}$ when between 400 – 500°C, as shown in Figure 2⁵. This complex oxide lies in the P63/mmc space group, a group of materials first synthesized by Shpanchenko et al.^{6,7}. Analogous complex oxides $\text{Ba}_5\text{Dy}_2\text{Al}_2\text{ZrO}_{13}$, $\text{Ba}_5\text{Tm}_2\text{Al}_2\text{ZrO}_{13}$, $\text{Ba}_5\text{Yb}_2\text{Al}_2\text{ZrO}_{13}$, and $\text{Ba}_5\text{Lu}_2\text{Al}_2\text{ZrO}_{13}$ were tested and displayed similar conductivity values, although $\text{Ba}_5\text{Lu}_2\text{Al}_2\text{ZrO}_{13}$ did not maintain high

conductivity at lower temperatures. Nearly a decade after the first discovery of proton conductivity in hexagonal perovskites with the 12R-type $\text{Sr}_3\text{LaNb}_3\text{O}_{12}$, 10L close-packed hexagonal perovskites were placed in the spotlight as intermediate temperature proton conductors.

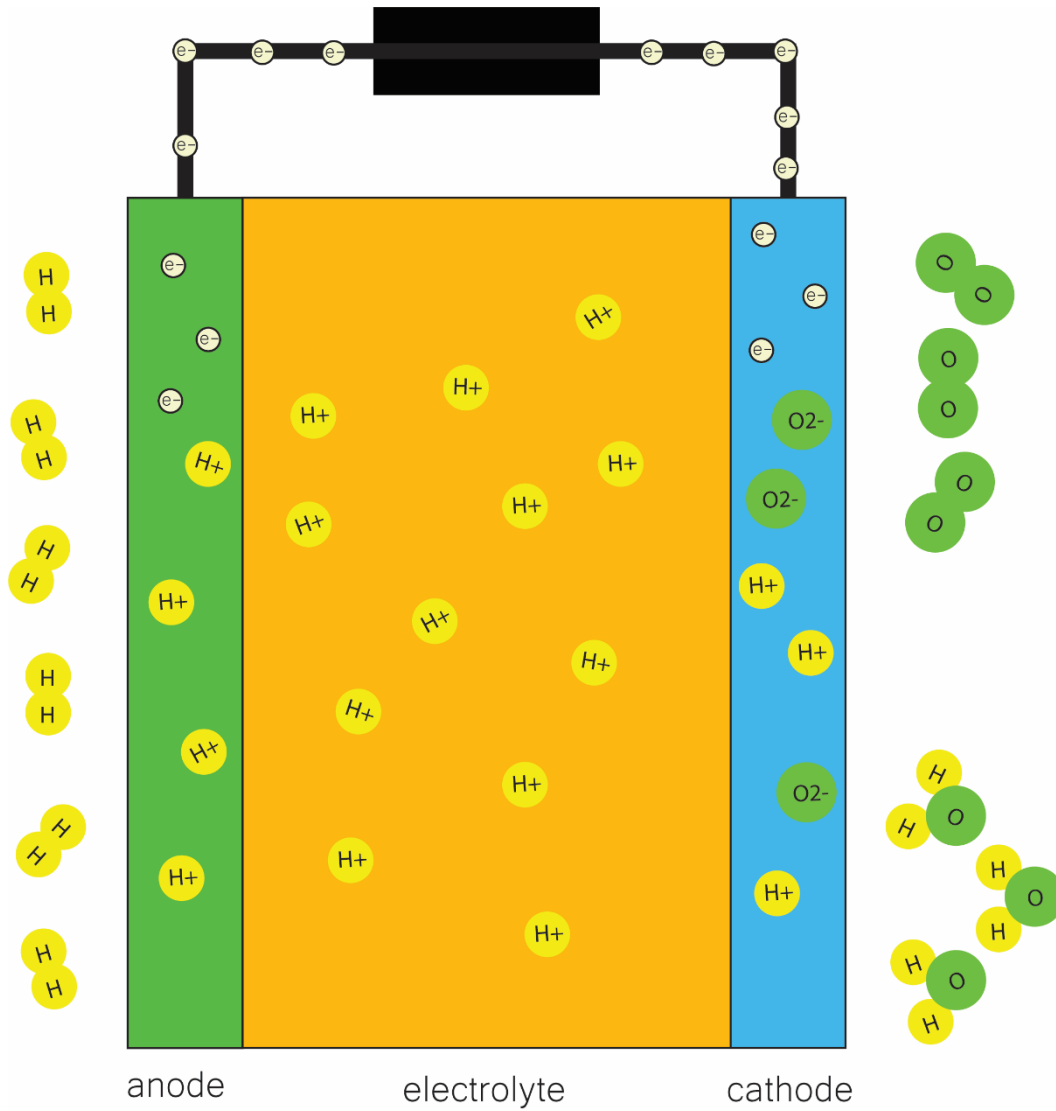


Figure 1. Simple model of PCFC

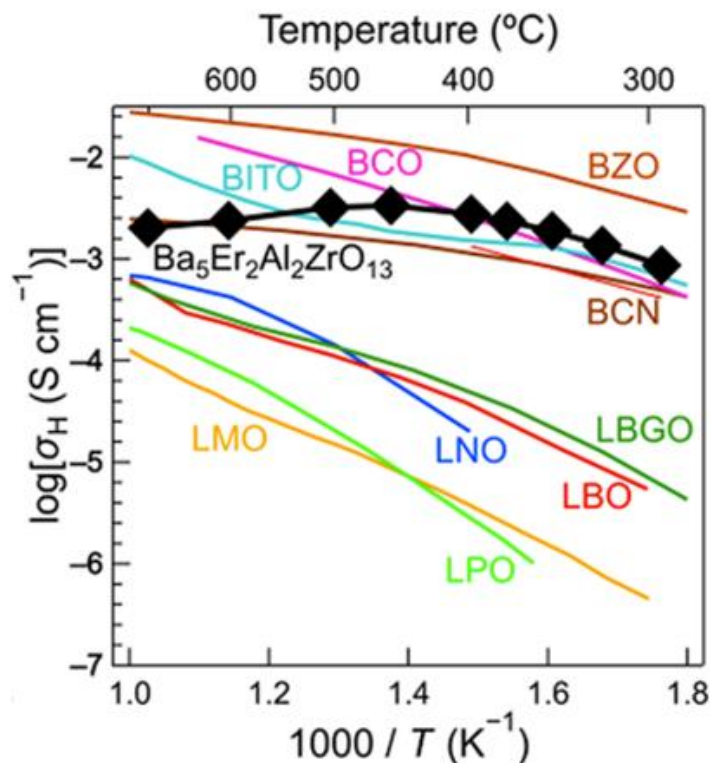


Figure 2. Comparison of BEAZ with other proton conductors. $\text{BaZr}_{0.8}\text{Y}_{0.2}\text{O}_{2.9}$ (BZO), $\text{BaCe}_{0.9}\text{Y}_{0.1}\text{O}_{2.95}$ (BCO), $\text{BaIn}_{1.6}\text{Ti}_{0.4}\text{O}_{5.2}$ (BITO), $\text{Ba}_3\text{Ca}_{1.18}\text{Nb}_{1.82}\text{O}_{8.73}$ (BCN), $\text{La}_{0.8}\text{Ba}_{1.2}\text{GaO}_{3.9}$ (LBGO), $\text{La}_{0.99}\text{Ca}_{0.01}\text{NbO}_{3.995}$ (LNO), $\text{La}_{26}\text{O}_{27}(\text{BO}_3)$ (LBO), $\text{La}_{5.4}\text{MoO}_{11.1}$ (LMO), $\text{La}_{0.9}\text{Sr}_{0.1}\text{PO}_{3.95}$ (LPO). Figure taken with permission from High Proton Conductivity in $\text{Ba}_5\text{Er}_2\text{Al}_2\text{ZrO}_{13}$, a Hexagonal Perovskite Related Oxide with Intrinsically Oxygen-Deficient Layers.⁵

Although BEAZ exhibited exceptional proton conductivity, little was understood about the proton uptake and migration in hexagonal perovskites. Murakami et al. attributed proton uptake to be a result of intrinsic oxygen vacancies in BEAZ, which allowed for proton-bonded oxygens to enter the system at oxygen vacancy sites⁵. In 2020 Fop et al. noted high dual oxide ion and proton conduction in hexagonal perovskite $\text{Ba}_7\text{Nb}_4\text{MoO}_{20}$, with bulk conduction reaching 4.0 mS cm^{-1} at 510°C ⁹. Much like BEAZ, the material's intrinsic anion vacancies were identified as the source of proton defects⁹. In 2023, Youn et al. proved experimentally that proton migration in BEAZ was preferential in the ab-plane by measuring conductivity in preferentially-

oriented samples¹⁰. Interestingly, DFT calculations showed that while proton uptake was energetically favorable in the oxygen-deficient O3 layer as predicted by Murakami et al., the energy barrier for proton uptake at the erbium/zirconium shared O2 layer was only 0.162 eV less stable. In addition, proton migration was found to be most energetically favorable along the octahedral O2 sites, in agreement with experimentally determined ab-plane preferred proton conductivity¹⁰.

In 2022, Andreev et al. first investigated the conductivity properties of analogous hexagonal perovskite Ba₅In₂Al₂ZrO₁₃ (BIAZ). Theorizing that increasing the In³⁺ and decreasing Zr⁴⁺ concentrations would increase the number of oxygen vacancies, increased indium content was found to be associated with larger values of proton uptake and total conductivity¹¹. Amongst investigated hexagonal perovskites capable of proton conduction, BEAZ remained the best intermediate temperature proton conductor. However, BIAZ is unique in this class of materials as it contains no paramagnetic ions. This important feature allows for BIAZ to be investigated through nuclear magnetic resonance, a meaningless experimental technique for the erbium containing BEAZ and most other P63/mmc hexagonal perovskites.

1.2 Experimental Methods

1.2.1 Solid-state Nuclear Magnetic Resonance (ss-NMR)

Ss-NMR is an element specific material characterization technique for solid phase samples. Samples of crushed powder are placed in a strong magnetic field, followed by application of radiofrequency pulses to manipulate a specific nucleus' magnetic dipole¹². The radiofrequency pulse applies a magnetic field oscillating close to the Larmor frequency of the

nucleus' magnetic spin, inducing a controlled change in the alignment of magnetic dipole¹³ as shown in Figure 3. Measuring relaxation time of the magnetic dipole's return to the permanent magnetic field orientation provides unique insight to the molecular structure surrounding the nuclei of interest. Any movement of charged particles near an atom, such as electrons and ions, distort the local magnetic field and impact the relaxation time of a specific atomic site; these site specific signals are represented via their respective chemical shift¹². NMR is a summation technique, where all nuclei of interest in a sample are accounted for in the data. The chemical shift of a nuclear signal gives insight to the chemistry and geometry surrounding an atomic site, while the relative area of each signal indicates the prevalence of the atomic site.

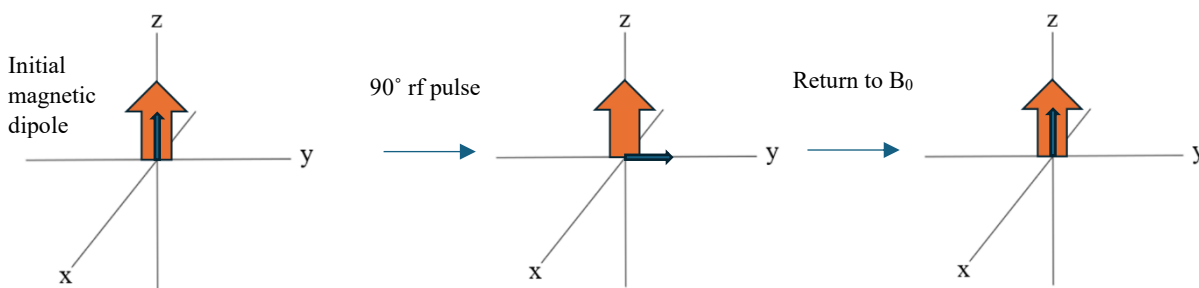


Figure 3. Representation of the permanent magnetic field B_0 (orange) and a sample's nuclear magnetic dipole (blue) in an NMR sequence. The dipole begins aligned with B_0 , followed by a radiofrequency pulse rotating the dipole, which then realigns itself to the permanent magnetic field.^{12,13}

1.2.2 Heteronuclear Correlation (HETCOR)

HETCOR NMR is a technique used to determine if two specific nuclei are spatially correlated. In the case of ^1H - ^{27}Al , homonuclear couplings are first removed from protons before transferring magnetization to the aluminum nucleus via cross polarization¹⁴. This provides a

through-space solution to cross polarization, which does not require bonding between the nuclei of interest¹⁴. The result of this technique is a two dimensional NMR plot, analyzed as a topographical map indicating peaks of spatially correlated nuclei at their correct respective chemical shifts. There can be concerns of proper chemical shift alignment, which are easy to correct if the spectrum contains multiple correlated signals but sometimes require extensive experimental work to resolve¹⁵.

1.2.3 Transfer of Populations in Double Resonance (TRAPDOR)

TRAPDOR NMR is a multiple resonance MAS experiment used to detect spatial correlation between a spin $\frac{1}{2}$ nucleus, typically protons, and a quadrupolar nucleus. By measuring the decay of the spin $\frac{1}{2}$ nucleus' signal with (S) and without irradiation (S_0) of the quadrupolar nucleus, heteronuclear dipolar coupling is selectively reintroduced¹⁶. which can cause signal distortion and decay. These distortions are typically removed by MAS NMR, however selective reintroduction results in a significantly quicker and more noticeable decay of spin $\frac{1}{2}$ nuclei signals experiencing the coupling effects of nearby quadrupolar nuclei. This technique allows for quantifiable measures of spatial correlation between nuclei via the TRAPDOR fraction shown in Equation 1, which expresses the impact of a quadrupolar nucleus on the proton signal decay.

$$\frac{S_0 - S}{S_0}$$

Equation 1.

The larger a signal's TRAPDOR fraction, the more protons from that site are spatially correlated to the quadrupolar nucleus¹⁷. This ultimately provides further insight to the surrounding chemistry of each spin $\frac{1}{2}$ signal.

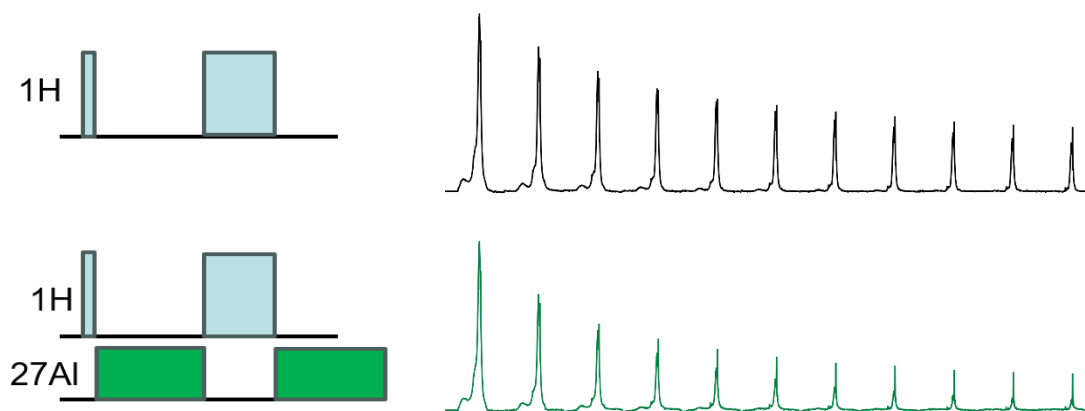


Figure 4. Example of ^1H - ^{27}Al TRAPDOR experiment, with the respective nuclear irradiation patterns and NMR spectra¹⁷

1.2.4 Multiple quantum magic angle spinning (MQMAS)

In magnetic dipoles of spin $\frac{1}{2}$ nuclei are impacted by dipolar couplings, as previously mentioned, but their interaction with the surrounding magnetic field is relatively simple. Nuclei with half-integer spins greater than one also experience quadrupolar coupling, which interact with the surrounding electric field gradient and further distorts ssNMR data. Quadrupolar coupling can be interpreted as variations to a nuclei's Zeeman interaction, with quantifiable perturbations specific to each spin transition and the order of coupling¹⁸.

First order quadrupolar coupling can be removed by high MAS frequencies, but second order interactions cause peak broadening that can't always be resolved in the presence of strong

magnetic fields^{12,19}. MQMAS overcomes second order interactions by manipulating spatial interactions to remove chemical shift anisotropy, dipolar couplings, and quadrupolar couplings, while having spin coherences evolve on different time scales. Classic NMR tests use a single pulse experimental approach, but by applying two rf pulses an isotropic echo can be detected and provide useful information on chemical shifts and peak broadening²⁰. Projecting the two time scales of spin evolutions onto direct and indirect dimensions produces a 2D plot with a clear isotropic chemical shift of nuclear signals, even in the presence of second order quadrupolar coupling.

1.2.5 Electrochemical Impedance Spectroscopy (EIS)

EIS compares input sinusoidal potential with output current and potential to understand how a material opposes the flow of current²¹. Application of AC signal creates sinusoidal voltage, leading to sinusoidal current, which is used to examine a material's impedance at varying voltage frequencies²². The relationship of voltage (E), current (I), angular frequency (ω), phase angle (φ), time (t), and impedance (Z), are described in equations 2-4.

$$E(t) = E\sin(\omega t)$$

Equation 2.

$$I(t) = I\sin(\omega t + \varphi)$$

Equation 3.

$$Z(t) = \frac{E(t)}{I(t)} = Z_0 \frac{\sin(\omega t)}{\sin(\omega t + \varphi)}$$

Equation 4.

Viewing impedance as a complex function is essential for understanding material behavior. Using Euler's formula impedance can be expressed by real and imaginary components, which represent the material's resistance and reactance, respectively²³.

$$Z(t) = Z_0 \exp(\cos\varphi + i\sin\varphi)$$

Equation 5.

$$\tan(\varphi) = \frac{Z_{Im}}{Z_{Re}}$$

Equation 6.

$$Z(\omega) = Z_{Re} - iZ_{Im}$$

Equation 7.

Plotting the change in impedance with changing voltage frequency is called a Nyquist plot, which provides information on a sample's bulk, grain boundary, and electrode resistance. The data can be fit to an equivalent electrical circuit, characterizing the behavior of charged particles in a material. With a well fit equivalent circuit, a sample's conductivity can be extracted from the computed resistance and measured geometry²². The relationship of voltage, current, resistance (R), conductivity (σ), sample thickness (l), and sample area (A) are described in equations 8-9.

$$R = \frac{E(t)}{I(t)}$$

Equation 8.

$$\sigma = \frac{1}{RA}$$

Equation 9.

By plotting conductivity against temperature, activation energies of conduction can be extracted based upon the Arrhenius equation²⁴. This is shown in Equation 10, describing the relationship of conductivity (σ), absolute temperature (T), frequency factor (A), activation energy (E_A), and universal gas constant (R).

$$\sigma T = A \exp\left(\frac{-E_A}{RT}\right)$$

Equation 10.

CHAPTER 2. BIAZ SYNTHESIS, CHEMISTRY, AND CRYSTAL STRUCTURE

2.1 Synthesis of BIAZ

BIAZ was synthesized via a solid-state synthesis route by adding precursors BaCO₃, In₂O₃, Al₂O₃, and ZrO₂ in their respective their stoichiometric proportions before a 24 hour ball mill in butanol-1. After drying the milling agent, the mixture underwent five 24 hour calcination steps in 100°C intervals from 800 - 1200°C, with intermediate grindings using mortar and pestle. After the calcining is completed, a final 10 hr 1475°C sintering step is required to achieve phase pure material. Pellets are prepared with 1.3 g of calcined powder mixed with three drops of 5% PVA solution (approximately 5:1 mass ratio) to reduce particle size, followed by drying for 30 min at 100°C. The powder was placed in a 15 mm die and pressed at 2000 PSI for 1 min, with a final 1 hr 200°C drying step to remove any remaining PVA before sintering.

2.2 Chemistry of BIAZ

To analyze the stoichiometry of BIAZ samples, inductively coupled plasma mass spectrometry (ICP-MS) and energy dispersive x-ray spectroscopy (EDX) were used to chemically analyze the compositions of BIAZ samples. ICP-MS tests were run twice on each sample, and EDX measured multiple points on pellet surfaces. ICP-MS and EDX results both agreed that the projected compositions were not successfully formed, with calculated stoichiometries shown in Table 1. The intended compositions of Ba₅In_{2+x}Al₂Zr_{1-x}O_{13-δ} (x = 0, 0.1, 0.2) were theorized to increase oxygen vacancy concentration by substituting In³⁺ for Zr⁴⁺, creating oxygen vacancies to preserve charge balance¹¹. Samples did not form the projected compositions or trend of indium, but a trend of increasing indium is observed as shown Table 1. Samples are referred to by the acronym and their respective indium content: BIAZ2.0, BIAZ2.6, BIAZ2.8.

Table 1. ICP-MS results of BIAZ samples, normalized to expected aluminum content

Nomenclature of sample	True Composition	Targeted composition
BIAZ2.0	$\text{Ba}_{4.22}\text{In}_{1.99}\text{Al}_2\text{Zr}_{0.85}\text{O}_{13}$	$\text{Ba}_5\text{In}_{2.2}\text{Al}_2\text{Zr}_{0.8}\text{O}_{13}$
BIAZ2.0	$\text{Ba}_{4.23}\text{In}_{1.93}\text{Al}_2\text{Zr}_{0.85}\text{O}_{13}$	$\text{Ba}_5\text{In}_{2.2}\text{Al}_2\text{Zr}_{0.8}\text{O}_{13}$
BIAZ2.6	$\text{Ba}_{5.12}\text{In}_{2.62}\text{Al}_2\text{Zr}_{1.10}\text{O}_{13}$	$\text{Ba}_5\text{In}_2\text{Al}_2\text{ZrO}_{13}$
BIAZ2.6	$\text{Ba}_{5.1}\text{In}_{2.52}\text{Al}_2\text{Zr}_{1.10}\text{O}_{13}$	$\text{Ba}_5\text{In}_2\text{Al}_2\text{ZrO}_{13}$
BIAZ2.8	$\text{Ba}_{5.04}\text{In}_{2.87}\text{Al}_2\text{Zr}_{1.0}\text{O}_{13}$	$\text{Ba}_5\text{In}_{2.1}\text{Al}_2\text{Zr}_{0.9}\text{O}_{13}$
BIAZ2.8	$\text{Ba}_{5.03}\text{In}_{2.7}\text{Al}_2\text{Zr}_{1.0}\text{O}_{13}$	$\text{Ba}_5\text{In}_{2.1}\text{Al}_2\text{Zr}_{0.9}\text{O}_{13}$

2.3 Crystal Structure of BIAZ

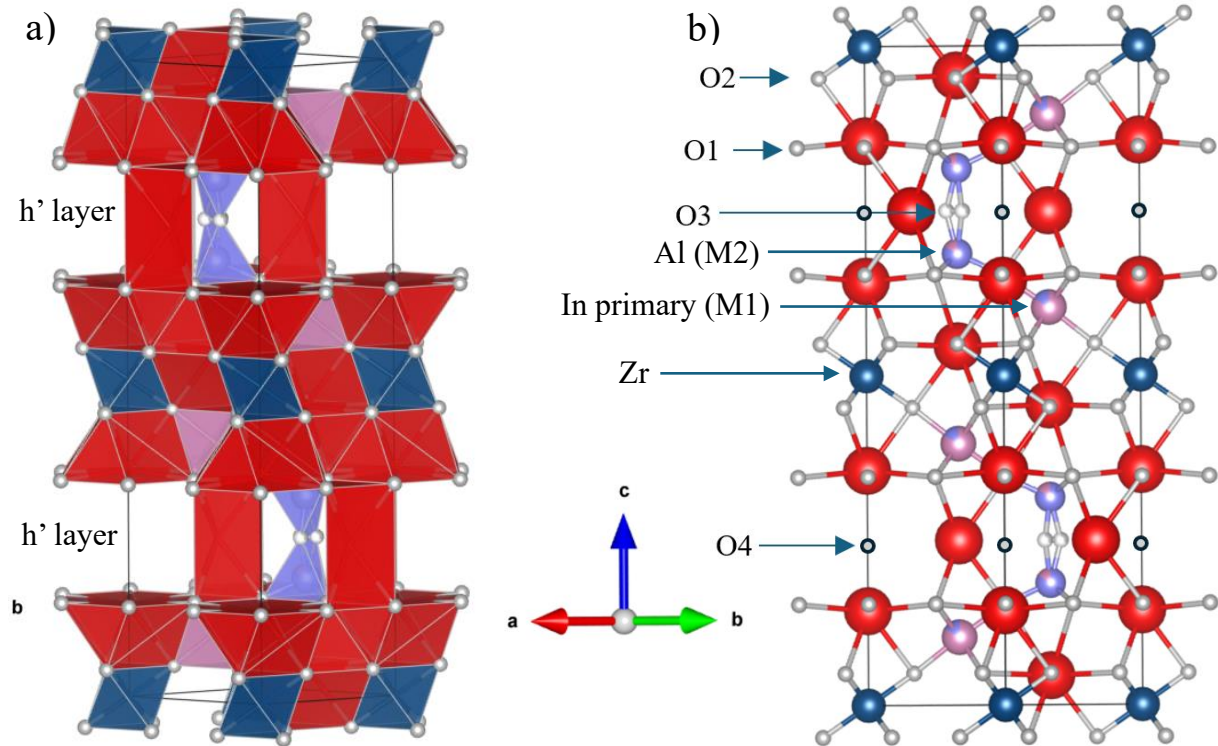


Figure 5. Unit cell of BIAZ from a) polyhedral perspective and b) atom/bond perspective. Barium, indium, aluminum, zirconium, and oxygen are red, pink, purple, blue, and white/gray, respectively. Images created using VESTA software, structural model created from Shpanchenko et al XRD refinement ⁶.

The crystal structure of BIAZ is a 10L close packing of BaO_{3-x} layers, which can be described as an intergrowth of alternating Ba₂InAlO₅ blocks and BaZrO₃ along the c-axis⁶, as shown in Figure 5. Indium and zirconium are in oxygen octahedra, while aluminum has a tetrahedral coordination due to the 1/3 occupancy of the O3 site⁶. Neutron powder diffraction (NPD) of BEAZ revealed a 20% occupancy of the O4 site in P63/mmc hexagonal perovskites⁵. Through refinement of XRD data, Shpanchenko et al. found aluminum and indium share two 4f Wyckoff positions: their respective sites have an Al:In statistical occupancy of 85:15 at $z = 0.397$ and 15:85 at $z = 0.815$ ⁶. Shpanchenko et al.'s conclusion of shared occupancy resolved concerns

with large thermal parameters (2.1 \AA^2 [In], -1.1 \AA^2 [Al]) when site swapping is unaccounted; reasonable thermal parameters and consistent statistical occupation are obtained when correcting the refinement ⁶.

2.3.1 XRD of BIAZ

Samples were analyzed via X-ray diffraction (XRD) at room temperature with $\text{CuK}\alpha$ radiation from $20^\circ - 60^\circ 2\Theta$ using a $2^\circ/\text{min}$ scanning rate. BIAZ falls in the $P63/mmc$ space group, and 100% phase pure samples were successfully synthesized as shown in *Figure 6*.

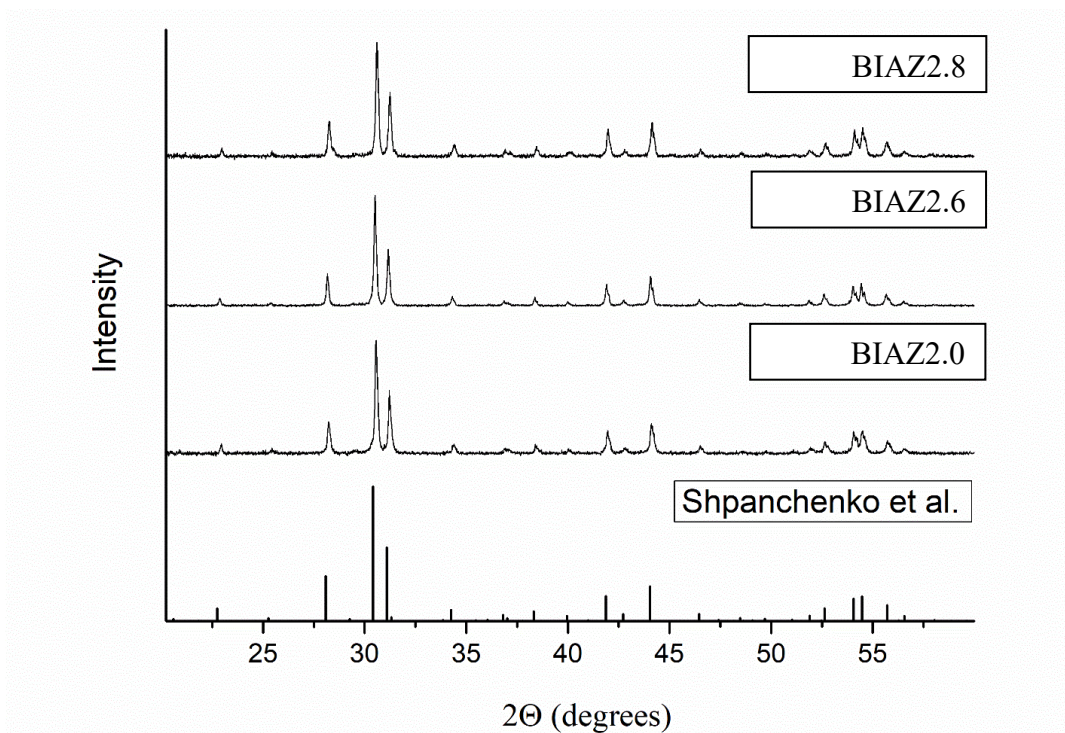


Figure 6. Diffractogram of varying BIAZ compositions and the BIAZ reference ⁶

Refinement of XRD data in this work, with an assumption of aluminum and indium sharing occupancy, agreed with the statistical occupancy reported by Shpanchenko et al. as shown in Figure 7. Lattice parameters listed in Table 2 were obtained via a Rietveld refinement of powder samples' XRD data, with multiple independent refinements conducted for confidence in results. The best fit parameters tabulated below achieved R-profile $\leq 10\%$.

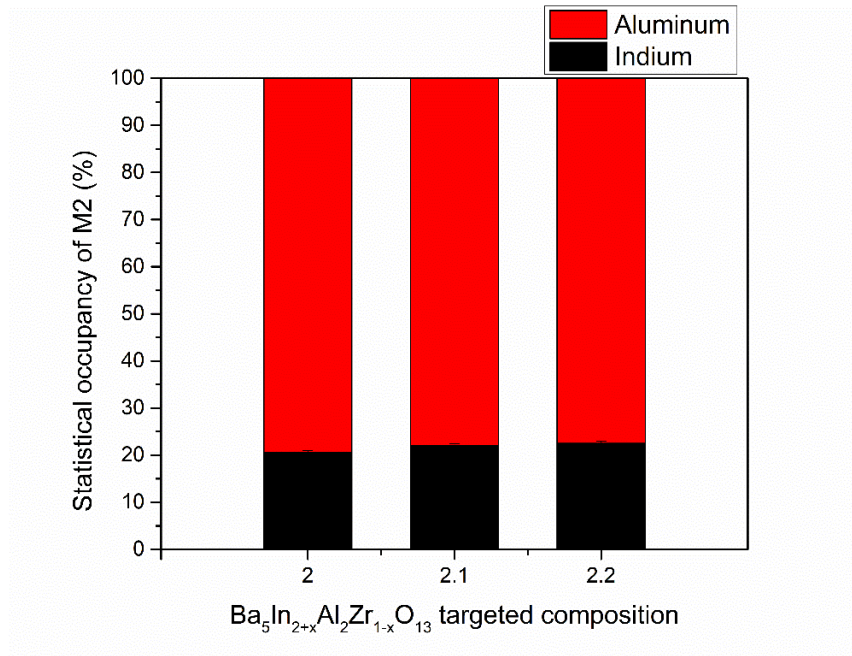


Figure 7. XRD refinement revealing statistical occupancy of the aluminum position ($z = 0.397$).. Samples defined by their projected stoichiometries.

Table 2. Lattice parameters of hexagonal perovskite BIAZ

material	a (Å)	b (Å)	c (Å)
BIAZ2.0 ^T	5.8691(2)	5.8691(2)	24.4139(11)
BIAZ2.0 ^S	5.8707(7)	5.8707(7)	24.455(3)
BIAZ2.0 ^A	5.967(2)	5.967(2)	24.006(8)
BIAZ2.1 ^A	5.970(1)	5.970(1)	24.011(4)
BIAZ2.6 ^T	5.8725(2)	5.8725(2)	24.3987(11)
BIAZ2.8 ^T	5.8675(1)	5.8676(1)	24.3896(7)

Note. T) this work. S) Shpanchenko et al.⁶ A) Andreev et al.¹¹

2.3.2 NPD of BIAZ

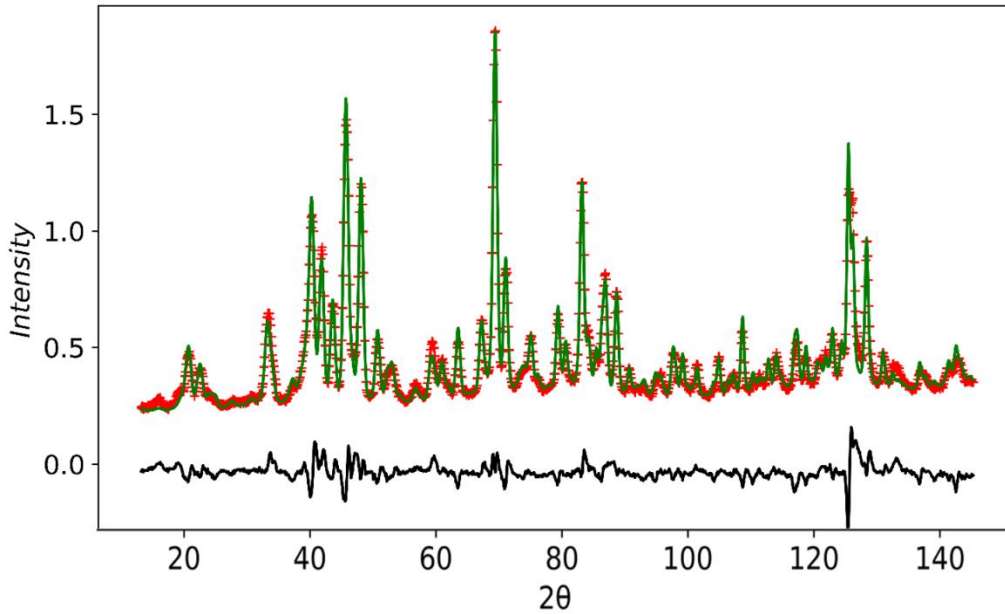


Figure 8. NPD diffractogram of BIAZ

Neutron diffraction was conducted on targeted sample composition BIAZ2.0, using approximately 2 g of sample placed in a 6 mm diameter V-Ni alloy can under a vacuum at 10^{-3} mbar. The sample was 100% phase pure, but no chemical analysis via ICPMS or EDX was conducted on the sample at the time of this work. No trends or conclusions were drawn between the projected indium content of this sample and subsequent results.

NPD identified the 4 expected oxygen sites seen in BEAZ, with an additional oxygen site located in the typically oxygen deficient h' layer. The new oxygen site, referred to as O5, sits at the same position along the c axis as O3. There are seven O5 sites located within the hexagonal layer with a calculated fractional occupancy of approximately 15%: three coordinating the indium site and four coordinating the adjacent barium. The refinement indicated fractional occupancy of O3, O4 and O5 sites, along with barium sites. O4 sites had a fractional occupancy

of approximately 17% and showed evidence of protonation, as expected from the BEAZ NPD refinements by Murakami et al. ⁵. Data was analyzed via a Le Bail refinement and subsequent Rietveld refinements. Fractional occupancies discussed were all shown to improve refinement of neutron diffraction data, and were done within reasonable expectations of the material based upon its precursors and previous literature. No other samples were tested through NPD due to time constraints.

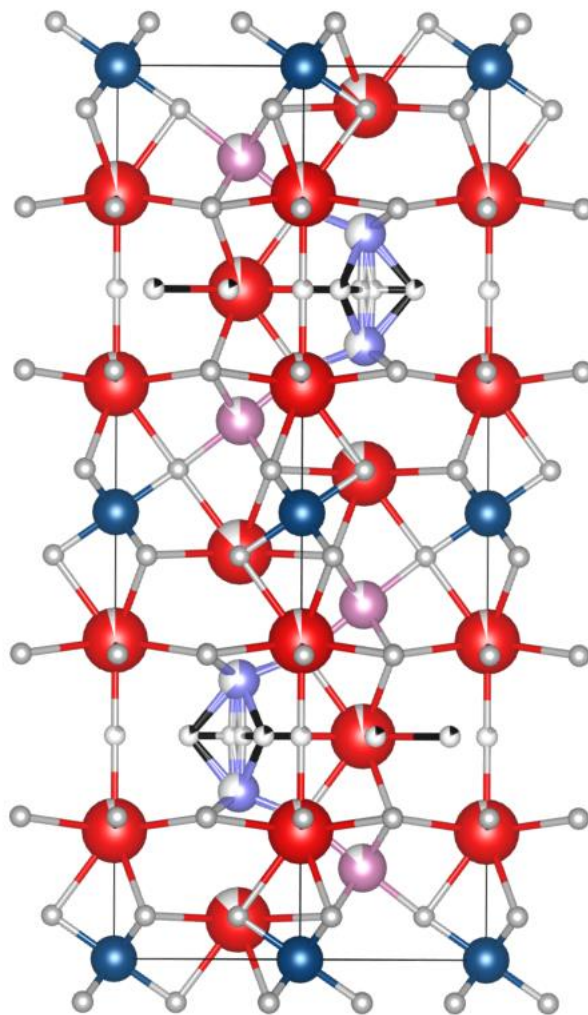


Figure 9. Refined BIAZ model based upon NPD and XRD results. Model produced in VESTA. Barium, indium, aluminum, zirconium, and oxygen are red, pink, purple, blue, and white/gray, respectively, with the O5 site highlighted in black.

2.4 Analysis of BIAZ structure and chemistry

The true compositions of BIAZ indicate the crystal structure can incorporate high levels of indium content. Previously BIAZ has been doped up with a 2.1:0.9 In:Zr ratio, or combinations of trivalent cations to create a 2.1:0.9 ratio with zirconium^{11,25,26}, but never to higher trivalent cation contents. For samples in this work, the In:Zr ratio increases with increasing indium content up to the maximum In/Zr proportion of 2.85. Given the XRD refinement and ICP-MS analysis, there is good evidence for successful substitution of indium for zirconium. Significant variations of the statistical site swapping are not seen with varying projected indium content, reducing the chances of higher indium content resulting from increased indium incorporation in the h' layer.

The unsuccessful synthesis of projected compositions indicates there are optimum indium concentrations at which BIAZ is best synthesized. Despite the achieving the highest indium concentrations ever reported, the synthesis approach was not controlled or studied in enough depth to probe the essential steps for precise BIAZ synthesis.

Based upon true compositions, increasing indium content was correlated with decreasing lattice constant along the c axis. Andreev et al. claimed to observe an increase in both the ab and c lattice constants with increasing indium content, but it was within the margin of error for their calculated values¹¹. The decreasing c parameter is beyond the margin of error for calculated values in this work. For the ab lattice parameter, no direct trend is observed with increasing indium content.

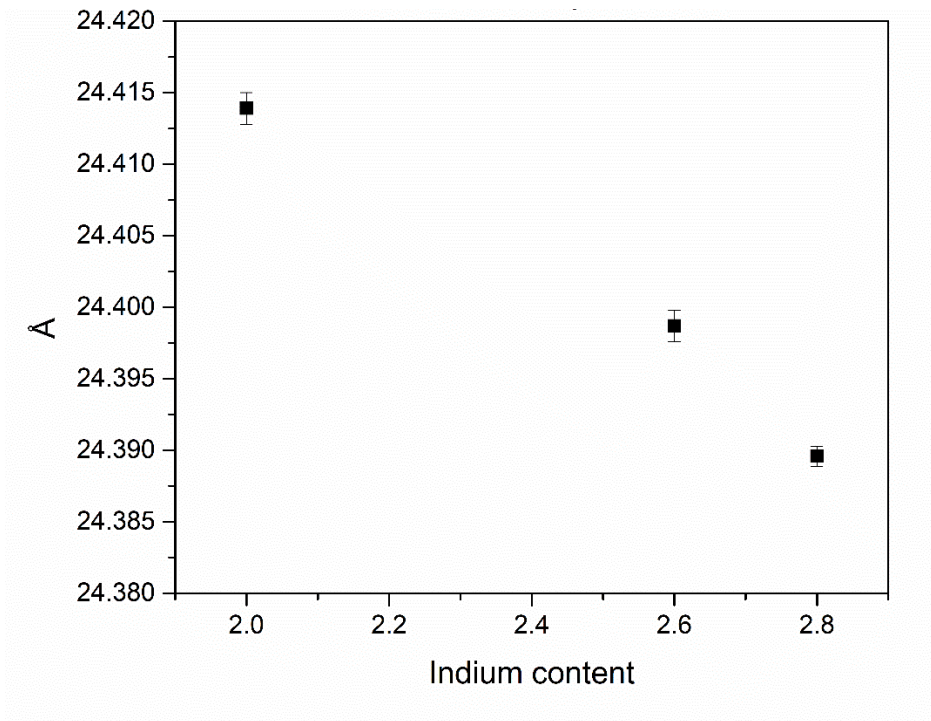


Figure 10. c-axis lattice constant of BIAZ with varying indium content

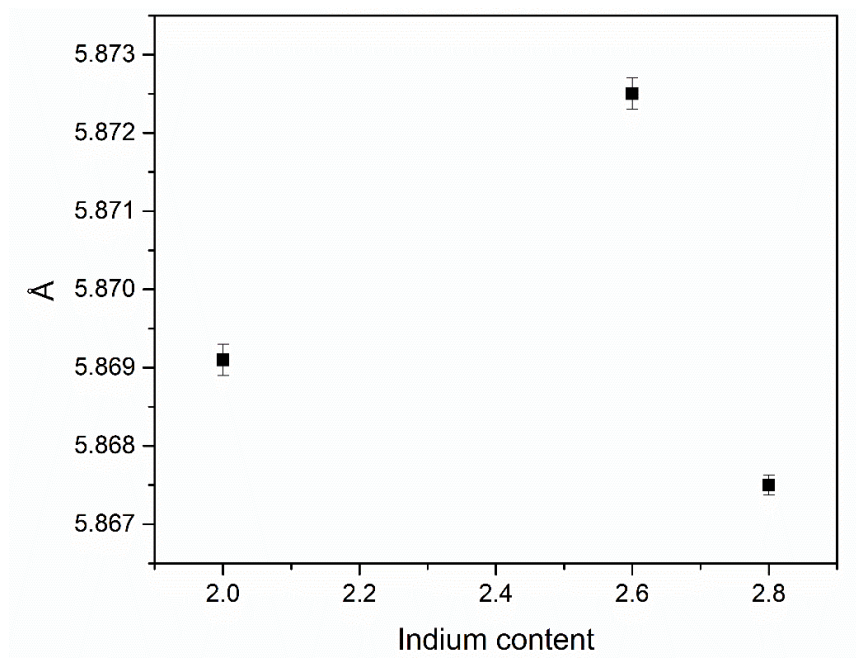


Figure 11. ab lattice constant of BIAZ with varying indium content

Based upon the O5 site's location and fractional occupancy, it is best attributed to coordinating oxygens of indium in the h' layer of BIAZ. This site is not observed in the similar $\text{Ba}_5\text{M}_2\text{Al}_2\text{ZrO}_{13}$ (M = Dy, Er, Tm, Yb, Lu) hexagonal perovskites investigated by Murakami et al. Since BIAZ is the only hexagonal perovskite with evidence of site swapping, and the fractional occupancy of the O5 site is approximately the same as the statistical site swapping of indium, there is strong evidence of this conclusion⁵⁻⁷. It is highly unlikely aluminum forms and coordinates to this O5 site.

Although the difference between projected and measured stoichiometry of BIAZ samples is surprising, the conflicting evidence for barium loss is also surprising. Neutron diffraction of indicated a 97% fractional occupancy of all barium sites, but stoichiometries calculated from ICP-MS and did not indicate a consistent barium loss.

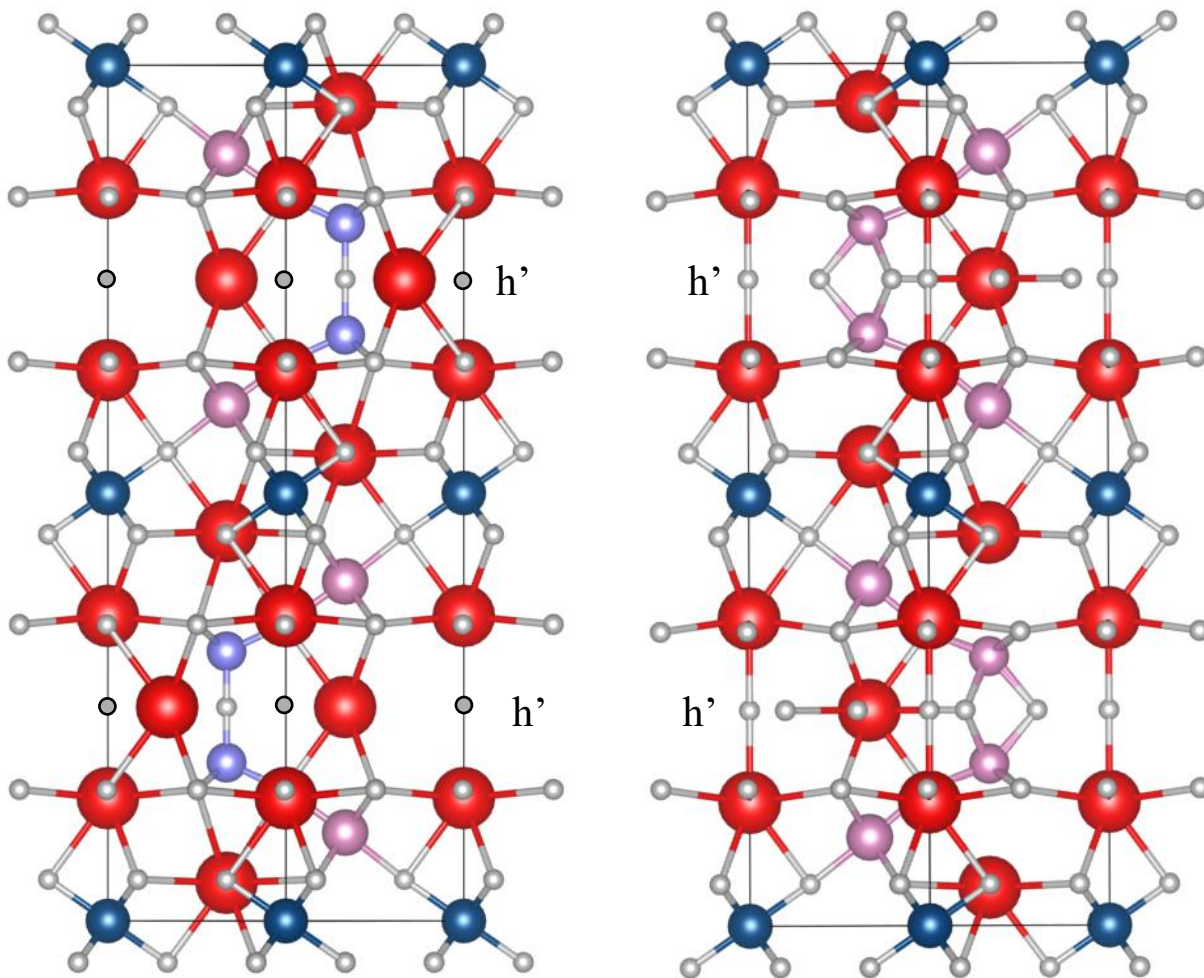


Figure 12. Majority and minority crystal structures of BIAZ based upon refinement. Full occupancy of atomic sites is used for clarity. Left) Majority structure BIAZ with a single O3 site in the h' layer coordinated by aluminum. Right) Minority structure BIAZ with O5 sites in the h' layer coordinating indium and barium. Barium, indium, aluminum, zirconium, and oxygen are red, pink, purple, blue, and white/gray, respectively. Models made using VESTA software.

With neutron diffraction evidence of indium creating the O5 site, the swapping of a single O3 site for the seven O5 sites in the h' layer could pose concerns for BIAZ's hydration capabilities. The h' layer is viewed as the oxygen deficient layer due to the intrinsically vacant O4 sites, which are filled when by oxygens accompanied by protons when exposed to water. The minority structure's h' layer is more densely packed due to the extra oxygens, which could affect

the associated energy barriers for hydration. Comparison of thermogravimetric analysis of BEAZ, which does not exhibit site swapping, and BIAZ, showed that BIAZ experiences insignificant mass change beyond 600°C, while BEAZ continues to lose mass up to 800°C^{5,11}. Assuming all mass loss resulted from water loss, this leads to the possibility of BIAZ being less capable of water incorporation. Alternatively, it could indicate a lower energy barrier for water loss or higher energy barrier for barium loss in BIAZ.

CHAPTER 3. NMR ANALYSIS OF BIAZ

3.1 Preparation of NMR samples and experimental conditions

NMR samples were prepared prior to those chemically analyzed through ICP-MS. Samples were prepared in an identical fashion, determined to be 100% phase pure, and there were no significant changes in NMR results between samples of different targeted compositions. For consistency of nomenclature, samples are referred to by the measured compositions discussed in section 2.2, assuming the identical synthesis process used in each targeted composition formed the same true composition. No trends, correlations, or conclusions were made between NMR results and sample's respective compositions.

Crushed powder samples of BIAZ2.0, BIAZ2.6, and BIAZ2.8 were analyzed using the following ss-NMR methods: ^1H NMR, ^{27}Al NMR, ^{17}O NMR, ^1H - ^{27}Al TRAPDOR NMR, and ^{17}O 3QMAS NMR. The natural abundance of ^1H , ^{27}Al , and ^{17}O are 99.99%, 100% and 0.038%, respectively ²⁷. ^{17}O is the only NMR-active oxygen nucleus, and due to their naturally low abundance samples were placed in a ^{17}O enriched O_2 atmosphere at 900°C for approximately 48 hours. To see the impact of proton uptake on the NMR signals of BIAZ, samples were also hydrated by bubbling argon through water at 400°C for one hour. Tests were conducted using an 11.7 Tesla magnet.

Table 3. Experimental matrix of NMR samples

Sample	^1H NMR	^{27}Al NMR	^1H - ^{27}Al HETCOR	^1H - ^{27}Al TRAPDOR	^{17}O NMR	^{17}O 3QMAS
BIAZ2.6 pristine	Tested	Tested				
BIAZ2.8 pristine	Tested	Tested				
BIAZ2.6 ^{17}O enriched					Tested	Tested
BIAZ2.0 ^{17}O enriched	Tested	Tested	Tested	Tested	Tested	
BIAZ2.6 hydrated	Tested	Tested	Tested	Tested		
BIAZ2.6 ^{17}O enriched + hydrated	Tested	Tested	Tested			

3.2 ^1H NMR

Proton NMR of BIAZ held consistent chemical shift values for varying indium compositions, with changes in the 7.5-8.5 ppm signal based upon sample preparation (Table 4). The broad signal detected at approximately 11 ppm is due to a fatty acid contaminant²⁸, obtained during the hydration process. This was confirmed via FTIR with the detection of carbonyls in hydrated samples. The known proton chemical shift region of carboxylic acids allowed for identification of the signal at 7.5 – 8.5 ppm. Oxygen enrichment decreased the total proton signal coming from 4.0 and 5.1 ppm peaks, while hydration increased the sum of their signals. 1.1 ppm and 0.7 ppm peaks were significantly reduced by all sample preparations.

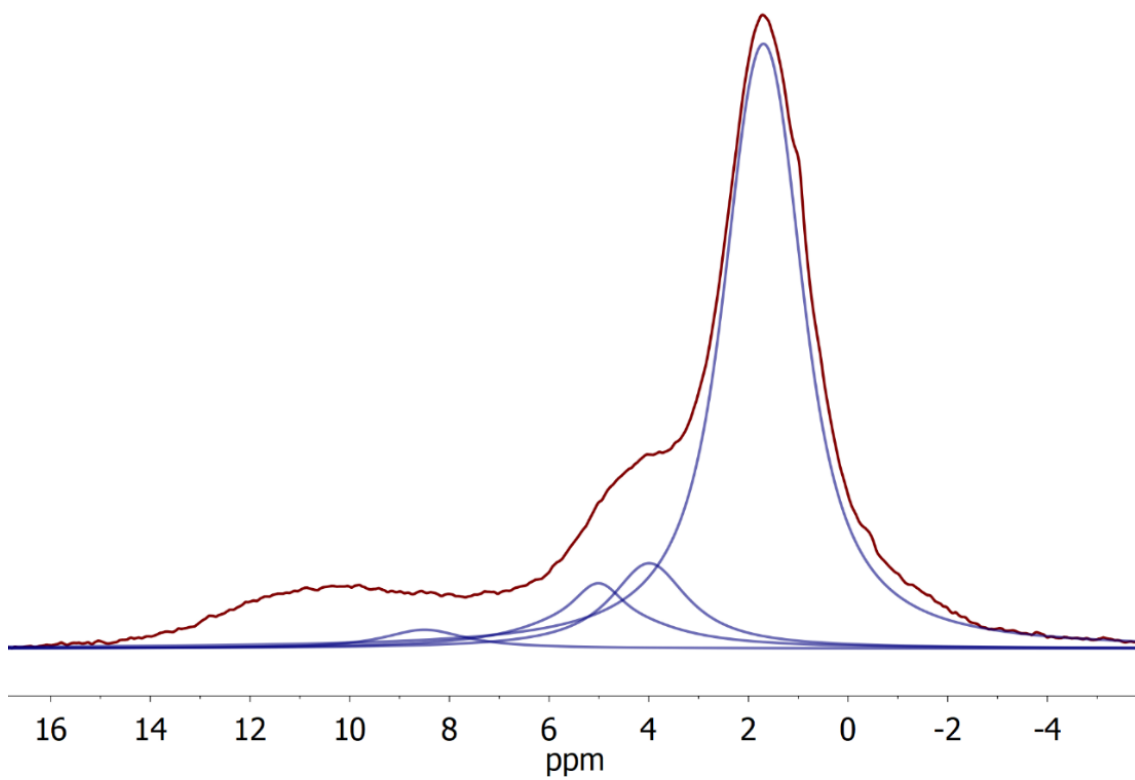


Figure 13. ^1H NMR fitted spectrum of hydrated BIAZ2.6 (MAS 22kHz).

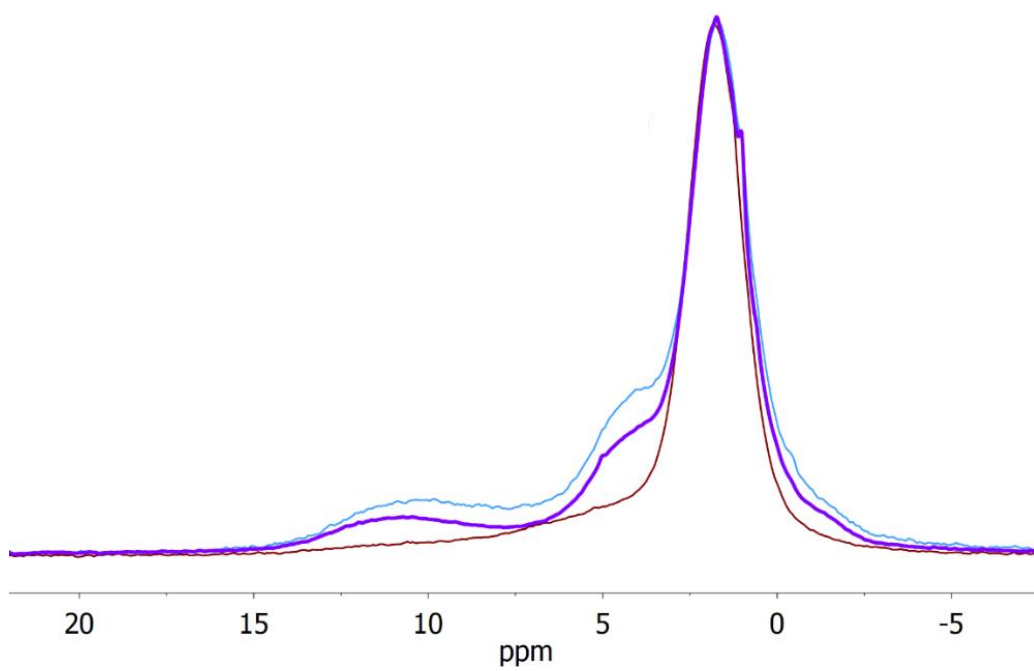


Figure 14. ^1H NMR of BIAZ2.6 with varying sample preparations (MAS 22kHz). Red, blue, and purple, are ^{17}O enriched, hydrated, and ^{17}O enriched + hydrated, respectively.

Table 4. ¹H NMR summary of BIAZ

BIAZ2.6 pristine	shift (ppm)	7.85	5.12	4.03	1.88	1.19	0.74
	relative area	4%	12%	3%	60%	15%	6%
BIAZ2.6 17O enriched	shift (ppm)	7.53	5.20	4.02	1.85	1.20	0.80
	relative area	2%	4%	5%	82%	4%	3%
BIAZ2.6 hydrated	shift (ppm)	8.50	5.01	3.99	1.70	0.99	0.60
	relative area	3%	9%	11%	74%	1%	2%
BIAZ2.6 17O enriched + hydrated	shift (ppm)	8.49	5.06	4.05	1.73	1.02	0.59
	relative area	2%	6%	3%	87%	2%	0%
BIAZ2.8 pristine	shift (ppm)	7.85	5.20	3.90	1.85	1.19	0.73
	relative area	8%	16%	8%	55%	8%	6%
BIAZ2.0 17O enriched	shift (ppm)	7.50	5.22	4.00	1.80	1.16	0.75
	relative area	3%	3%	2%	83%	6%	4%

3.3 ^{27}Al NMR

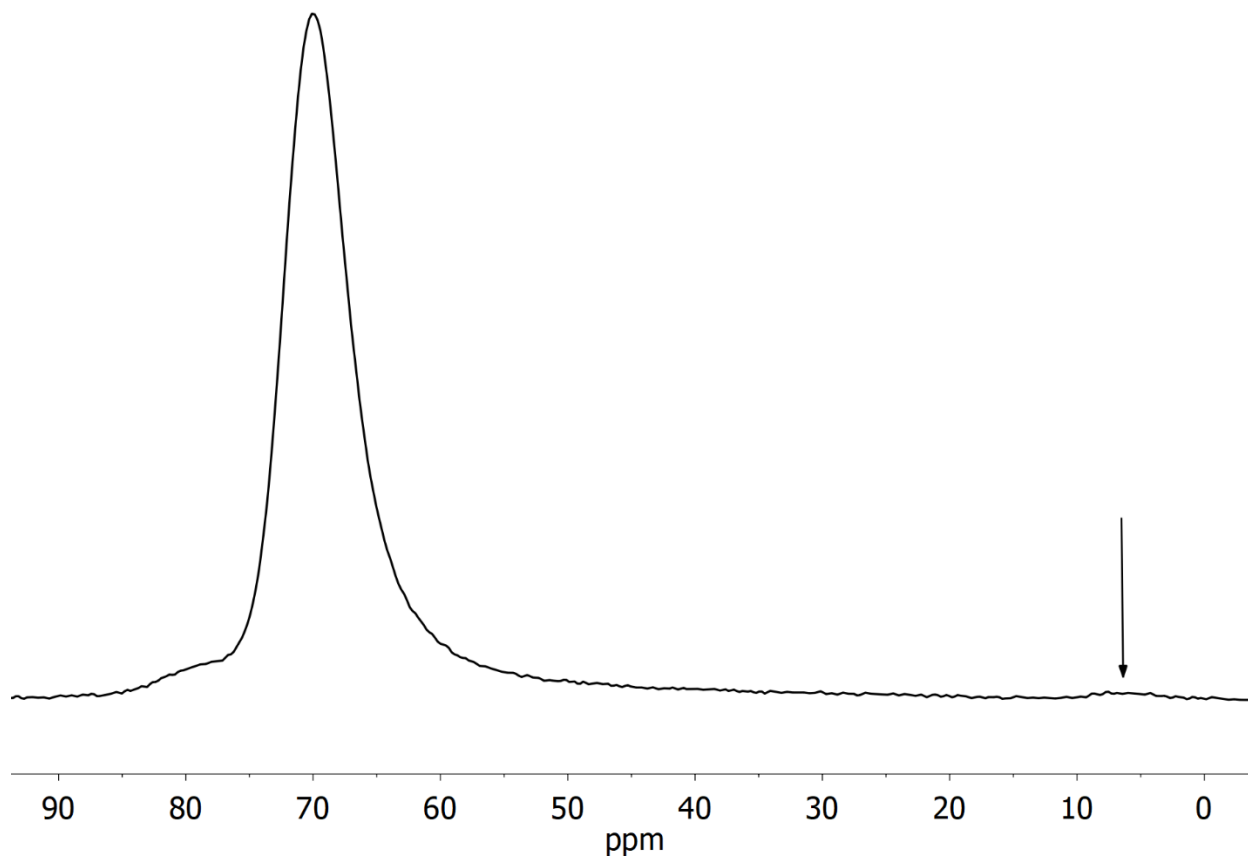


Figure 15. ^{27}Al NMR of BIAZ2.6 (MAS 18kHz), 6.2 ppm peak indicated by arrow

^{27}Al NMR of BIAZ did not reveal significant changes due to variations of indium composition. Pristine and ^{17}O enriched BIAZ had 98-99% of detected nuclei at the 70 ppm shift, with trace quantities observed around 6 ppm as shown in Figure 15. Samples that underwent hydration or ^{17}O enrichment did not show any 6 ppm signals, as seen in Table 5. Second order quadrupolar coupling constants were experimentally determined to be around 1.8 MHz for pristine and ^{17}O enriched samples, and approximately 1.6 MHz for hydrated samples, with no changes observed due to varying indium content (Table 5). All samples' C_q were best fit with

asymmetry parameter $\eta = 1$. Fittings were done using DMFit software with a 2nd order quadrupolar coupling model. C_q and relative errors were obtained by averaging multiple independent fittings of spectra. Application of a secondary Czjzek model ($C_q = 3.27$ MHz), which was made to model NMR data of statistically disordered structures²⁹, improved all fittings.

Table 5. ²⁷Al NMR parameters of BIAZ

Sample	BIAZ2.6 pristine	BIAZ2.8 pristine	BIAZ2.0 17O enriched	BIAZ2.6 hydrated	BIAZ2.8 17O enriched + hydrated
chemical shift (relative area)	70 ppm (99%)	70 ppm (98%)	70 ppm (99%)	68.5 ppm (100%)	68.2 ppm (100%)
	6.2 ppm (1%)	6.2 ppm (2%)	6.2 ppm (1%)	N/A	N/A
2 nd C _q (MHz)	1.85 (±0.15)	1.83 (±0.2)	1.8 (±0.2)	1.62 (±0.1)	1.6 (±0.15)

3.4 2D ¹H-²⁷Al NMR

3.4.1 ¹H-²⁷Al HETCOR NMR

Heteronuclear correlation of BIAZ identified the 5.1 ppm proton signal to be spatially correlated to tetrahedral aluminum in both tests conducted. In the ¹⁷O enriched BIAZ2.0 sample, the 1.8 ppm proton signal was also correlated to aluminum, however this was not seen in hydrated BIAZ2.6. This discrepancy, along with the inaccurate 1H NMR trace resolved from the ¹⁷O enriched BIAZ2.6 DATA, raised concerns of chemical shift scaling for the proton dimension. This will be addressed in further detail in section 3.6.

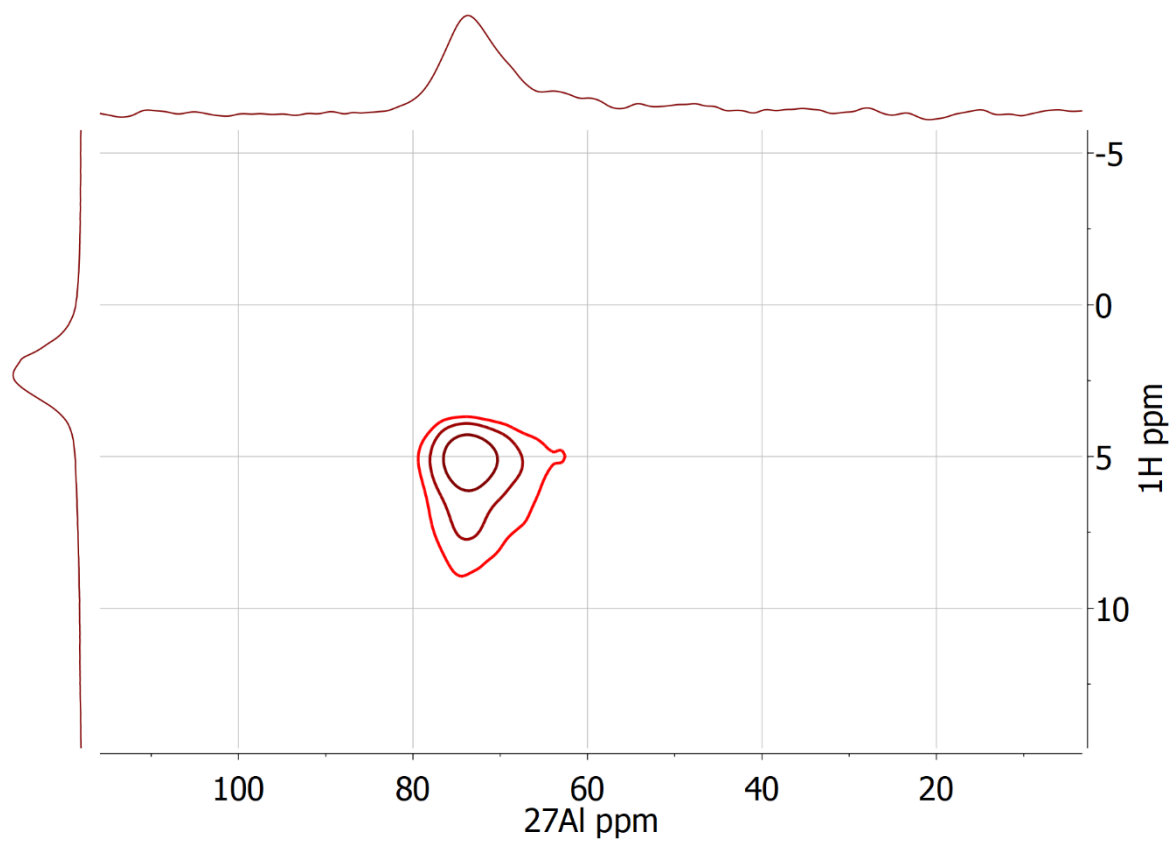


Figure 16. ^1H - ^{27}Al HETCOR NMR of hydrated BIAZ2.6

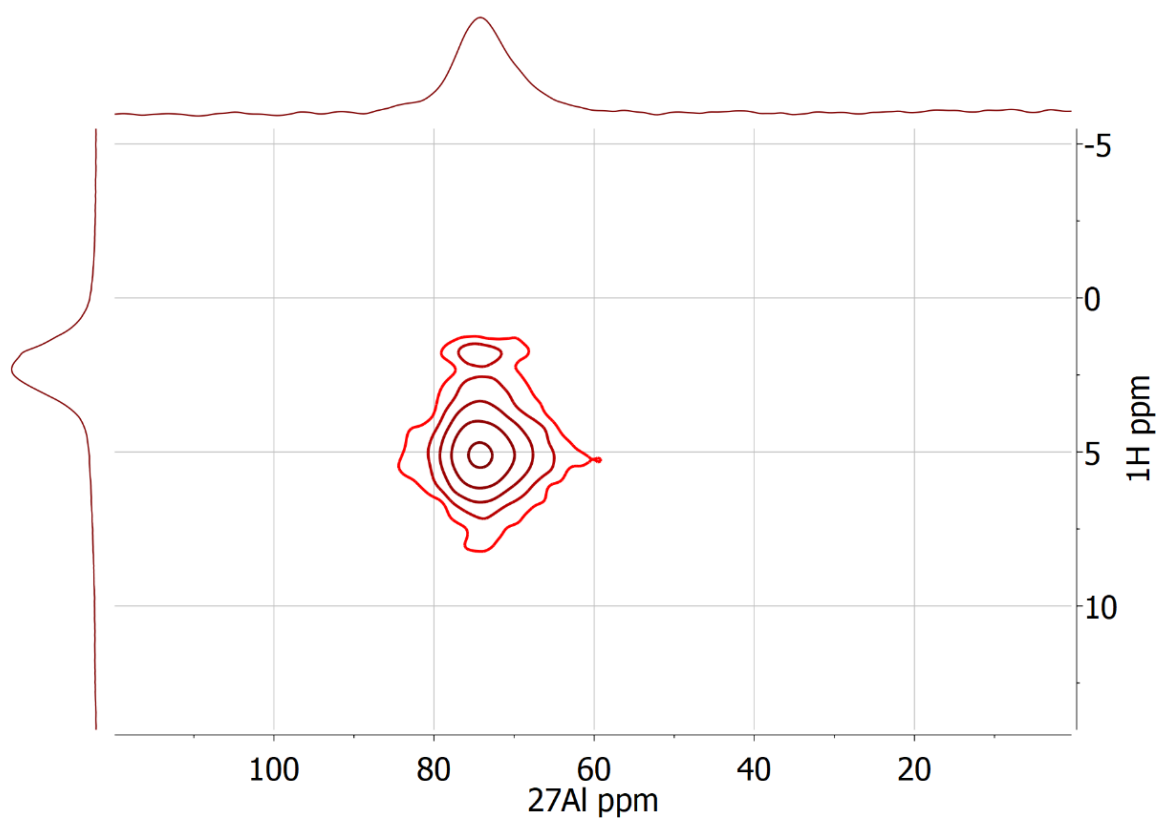


Figure 17. ^1H - ^{27}Al HETCOR NMR of ^{17}O enriched BIAZ2.0

3.4.2 ^1H - ^{27}Al TRAPDOR NMR

To determine the proximity of specific proton signals to aluminum nuclei, ^1H - ^{27}Al TRAPDOR NMR was used. Due to inconsistent phasing of the echo signals, TRAPDOR fractions were not able to be calculated for 8.5, 5.1 and 4.0 signals. To determine which signals were most impacted by the reintroduction of ^{27}Al heteronuclear couplings, individual TRAPDOR fractions were compared with a TRAPDOR fraction of the entire spectrum.

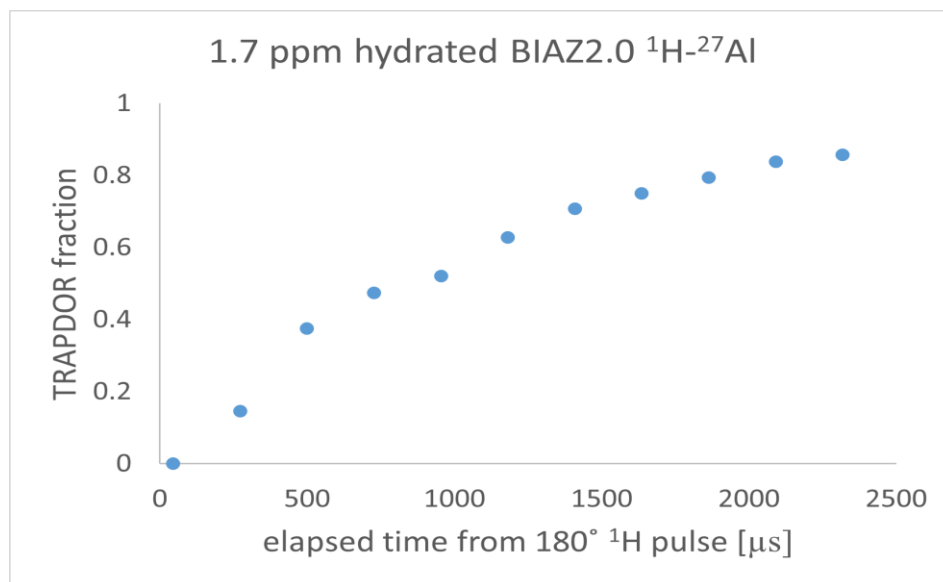


Figure 18. Example of attainable ^1H - ^{27}Al TRAPDOR fraction of BIAZ

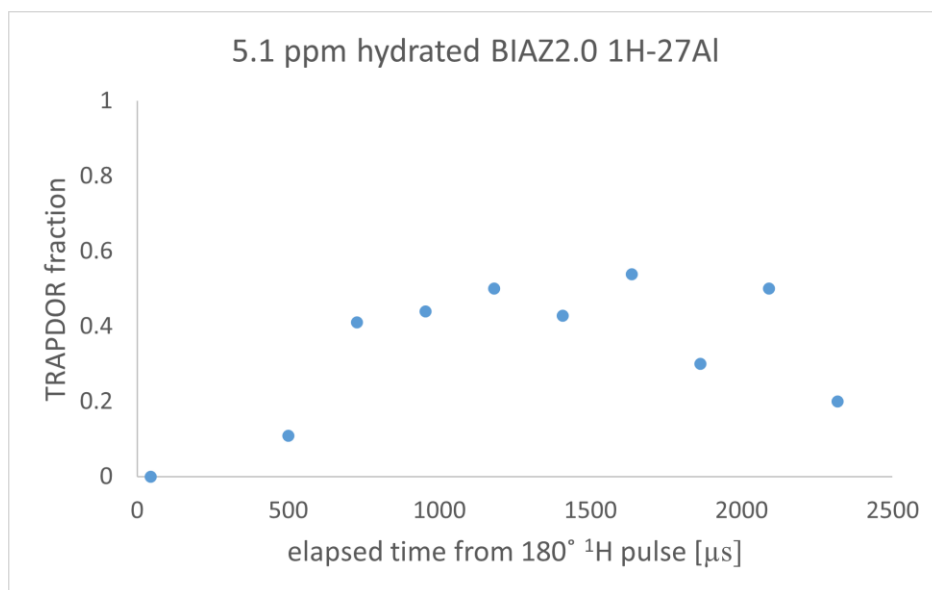


Figure 19. Example of unattainable ^1H - ^{27}Al TRAPDOR fraction of BIAZ

Table 6. ^1H - ^{27}Al TRAPDOR fractions of proton signals in BIAZ

	Whole Signal	1.7 ppm	1.0 ppm	0.6 ppm
BIAZ2.6 hydrated	0.68	0.85	0.70	0.65
BIAZ2.6 enriched + hydrated	0.65	0.85	0.48	0.69
BIAZ2.0 enriched	0.93	0.98	0.81	0.82

The closer a signal's TRAPDOR fraction is to one, the more protons of that site are spatially correlated to aluminum ¹⁷. Comparing with the whole signal gives strong evidence the 1.7 ppm signal's decay was impacted by aluminum nuclei, while other measurable proton signals' echo decay is not impacted by aluminum.

3.5 ^{17}O 1D and ^{17}O 3QMAS NMR

3.5.1 1D ^{17}O NMR

^{17}O -enriched samples were prepared and tested using ^{17}O NMR, with no detectable change in nuclear signals due to changes in indium composition. However, the complex spectrum was difficult to discern in one dimension. 3QMAS NMR was needed to properly identify all nuclear signals in the spectrum, although it provided little improvement in analysis of the spectrum. Concentration of oxygen signals is directly proportional to their relative area, listed in Table 7

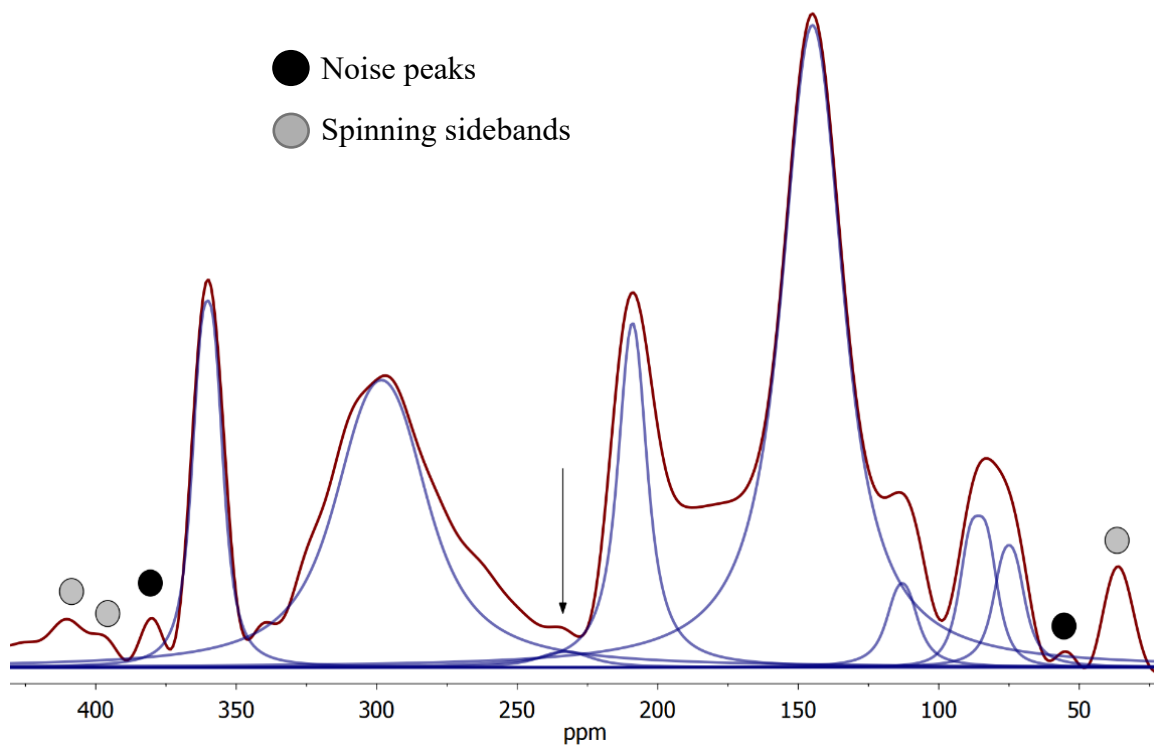


Figure 20. 1D ^{17}O NMR of ^{17}O enriched BIAZ2.6 (MAS 22kHz). Black arrow points out real 233 ppm ^{17}O signal.

3.5.2 3QMAS ^{17}O NMR

3QMAS ^{17}O NMR manipulates the $+3/2$ to $-3/2$ transition, rather than the common $+1/2$ to $-1/2$ transition, to identify a sample's nuclear signals without quadrupolar broadening³⁰. The 2D plot is a topographical map of the NMR spectrum, with ^{17}O peaks visible along the diagonal chemical shift axis and quadrupolar induced shifts causing a displacement of the signal's center of gravity³⁰. The experiment led to the discovery of the small 231 ppm peak, and confirmed the signal detected between 208 and 144 ppm peaks was a real product of the 208 ppm peak.

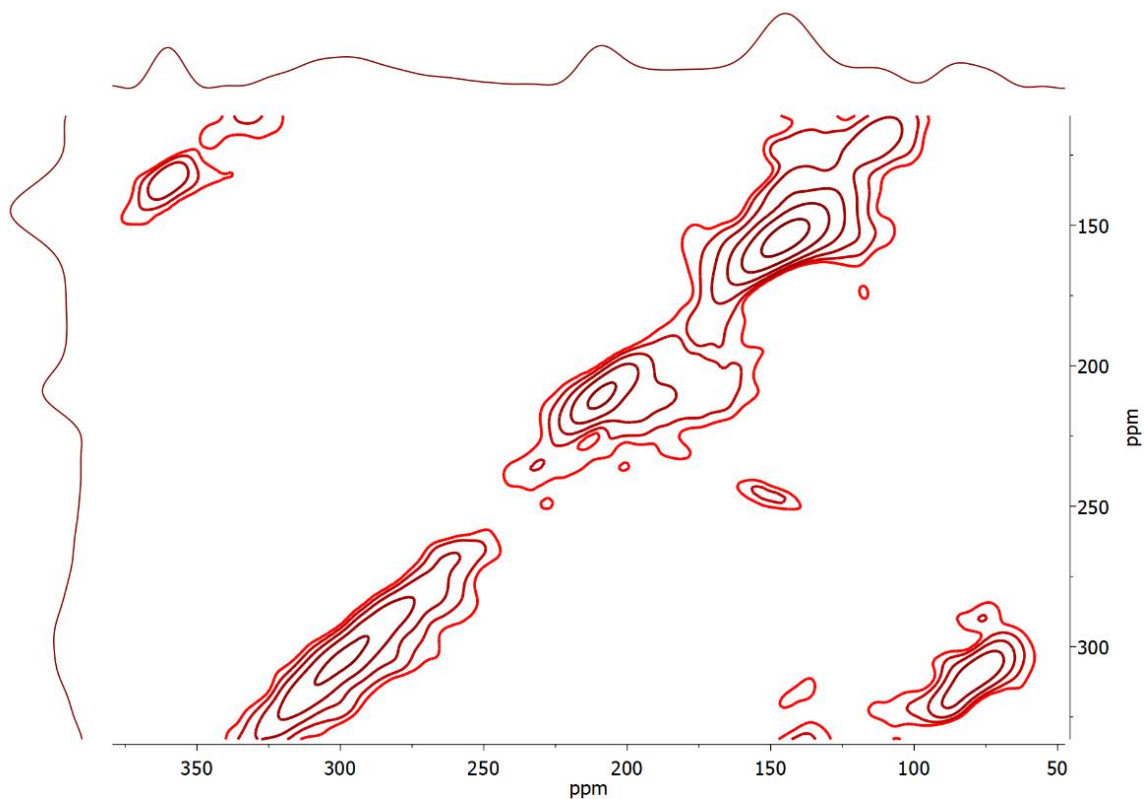


Figure 21. ^{17}O 3QMAS NMR of BIAZ2.6 (MAS 22kHz)

Table 7. Summary of ^{17}O signals detected in BIAZ

^{17}O enriched BIAZ2.6	shift (ppm)	60	298	209	233	145	113	86	75
	relative area	10%	26%	11%	1%	42%	3%	4%	3%
^{17}O enriched BIAZ2.0	shift (ppm)	361	302	210	231	147	114	88	78
	relative area	9%	27%	13%	1%	43%	1%	3%	2%

3.6 Discussion of NMR results

3.6.1 ^1H NMR

The proton signals detected in BIAZ align with expected chemical shifts in proton conducting hexagonal perovskites⁸ and barium indium oxides³¹. Based upon the HETCOR and TRAPDOR NMR results, the 5.1 ppm signal and 1.8 ppm signals have strong evidence as protons spatially correlated to aluminum. The high ^1H - ^{27}Al TRAPDOR fraction of the 1.8 ppm proton signal measured in all samples provide more confidence in the HETCOR signals' chemical shift excellent alignment at 5.1 ppm and 1.8 ppm. Fitting the ^1H spectrum with these chemical shifts yields the most consistent fitting results, providing more confidence in the determination of ^1H - ^{27}Al correlated signals at these chemical shifts. The higher a chemical shift value in ^1H NMR, the more acidic the associated proton site⁸. Comparing the two ^1H - ^{27}Al correlated signals, 5.1 ppm signal is best attributed to O3-O4 bonded protons based upon the acidity of its position. This follows the same logic as Tabacaru et al.'s analysis of ^1H NMR in the 12R type hexagonal perovskite, which attributed the 5 ppm detected signal to the most acidic site⁸. By assigning the 5.1 ppm signal to O3-O4 bonded protons, the 1.8 ppm signal is best attributed to O1 bonded protons given the position's proximity to aluminum nuclei.

Given the best assignment of the 5.1 ppm and 1.8 ppm signals, the 4.0 ppm signal was investigated as O2 bonded protons lying in BIAZ's barium zirconate (BZO) layer. Previous work ^1H NMR of 20% yttrium doped BZO by Blanc et al. found proton signals at 5.4 and 6.8 ppm, with theoretically calculated chemical shifts predicted at 4.5 and 6.8 respectively³² as shown in

Table 8

Material	Nucleus of interest	Crystal structure	Configuration or Coordination	Observed chemical shift	Calculated chemical shift	Source
Ba ₂ In ₂ O ₄ (OH) ₂	17O	tetragonal	unprotonated oxygen, proton acceptor oxygen, proton donor oxygen	140, 174, 192, 207	197-223, 204-225, 169-185, 137-171	Dervisoglu et al. ³¹
BaZrO ₃	17O	Cubic	4 planar barium, 2 linear zirconium	376		Bastow et al. ³⁶
SrZrO ₃	17O	Orthorhombic	3 strontium, 2 zirconium	343/340		Bastow et al. ³⁶
CaZrO ₃	17O	Orthorhombic	3 calcium, 2 zirconium	336/329		Bastow et al. ³⁶
BaTiO ₃	17O	tetragonal	4 planar barium, 2 linear titanium	564/523		Bastow et al. ³⁶
SrTiO ₃	17O	Cubic	4 planar strontium, 2 linear titanium	465		Bastow et al. ³⁶
Al ₂ O ₃ Θ-phase	27Al	monoclinic	octahedral	10.5	11.3	Choi et al. ³⁷
Al ₂ O ₃ Θ-phase	27Al	monoclinic	tetrahedral	80	79.5	Choi et al. ³⁷
BZY20	1H	cubic	Yttrium 1st & 2nd oxygen neighbor	5.4, 6.8	4.5, 6.8	Blanc et al. ³²
BZSc5	1H	cubic	Scandium 1st oxygen neighbor	4.4		Buannic et al. ³³
BZSc15	1H	cubic	Scandium 1st oxygen neighbor	4	3.7-4.9	Buannic et al. ³³
BZSc30	1H	cubic	Scandium 1st oxygen neighbor	3.3		Buannic et al. ³³
Sr ₃ LaNbO ₁₂	1H	hexagonal	1 Nb-O 3 Sr/La-O bonds, 2 Nb-O 2 Sr/La-O bonds	5, 3.4, 1.3		Tabacaru et al. ⁸
Ba ₂ In ₂ O ₄ (OH) ₂	1H	tetragonal	planar O-H-O, cross-plane O-H-O	7.3, 3.3, 1.7	8.5-9.7, 3.8 - 5.3	Dervisoglu et al. ³¹

Material	Nucleus of interest	Crystal structure	Configuration or Coordination	Observed chemical shift	Calculated chemical shift	Source
Ba ₂ In ₂ O ₄ (OH) ₂	17O	tetragonal	unprotonated oxygen, proton acceptor oxygen, proton donor oxygen	140, 174, 192, 207	197-223, 204-225, 169-185, 137-171	Dervisoglu et al. ³¹
BaZrO ₃	17O	Cubic	4 planar barium, 2 linear zirconium	376		Bastow et al. ³⁶
SrZrO ₃	17O	Orthorhombic	3 strontium, 2 zirconium	343/340		Bastow et al. ³⁶
CaZrO ₃	17O	Orthorhombic	3 calcium, 2 zirconium	336/329		Bastow et al. ³⁶
BaTiO ₃	17O	tetragonal	4 planar barium, 2 linear titanium	564/523		Bastow et al. ³⁶
SrTiO ₃	17O	Cubic	4 planar strontium, 2 linear titanium	465		Bastow et al. ³⁶
Al ₂ O ₃ Θ-phase	27Al	monoclinic	octahedral	10.5	11.3	Choi et al. ³⁷
Al ₂ O ₃ Θ-phase	27Al	monoclinic	tetrahedral	80	79.5	Choi et al. ³⁷
BZY20	1H	cubic	Yttrium 1st & 2nd oxygen neighbor	5.4, 6.8	4.5, 6.8	Blanc et al. ³²
BZSc5	1H	cubic	Scandium 1st oxygen neighbor	4.4		Buannic et al. ³³
BZSc15	1H	cubic	Scandium 1st oxygen neighbor	4	3.7-4.9	Buannic et al. ³³
BZSc30	1H	cubic	Scandium 1st oxygen neighbor	3.3		Buannic et al. ³³
Sr ₃ LaNbO ₁₂	1H	hexagonal	1 Nb-O 3 Sr/La-O bonds, 2 Nb-O 2 Sr/La-O bonds	5, 3.4, 1.3		Tabacaru et al. ⁸
Ba ₂ In ₂ O ₄ (OH) ₂	1H	tetragonal	planar O-H-O, cross-plane O-H-O	7.3, 3.3, 1.7	8.5-9.7, 3.8 - 5.3	Dervisoglu et al. ³¹

Table 8. Similarly, Buannic et al. observed proton signals in scandium doped BZO between 4.4 and 3.3 ppm, where lower chemical shifts were related to increased scandium content³³, as shown in

Table 8. Based upon these trends in proton chemical shifts for 3+ cation doped BZO structures,

Material	Nucleus of interest	Crystal structure	Configuration or Coordination	Observed chemical shift	Calculated chemical shift	Source
Ba ₂ In ₂ O ₄ (OH) ₂	17O	tetragonal	unprotonated oxygen, proton acceptor oxygen, proton donor oxygen	140, 174, 192, 207	197-223, 204-225, 169-185, 137-171	Dervisoglu et al. ³¹
BaZrO ₃	17O	Cubic	4 planar barium, 2 linear zirconium	376		Bastow et al. ³⁶
SrZrO ₃	17O	Orthorhombic	3 strontium, 2 zirconium	343/340		Bastow et al. ³⁶
CaZrO ₃	17O	Orthorhombic	3 calcium, 2 zirconium	336/329		Bastow et al. ³⁶
BaTiO ₃	17O	tetragonal	4 planar barium, 2 linear titanium	564/523		Bastow et al. ³⁶
SrTiO ₃	17O	Cubic	4 planar strontium, 2 linear titanium	465		Bastow et al. ³⁶
Al ₂ O ₃ Θ-phase	27Al	monoclinic	octahedral	10.5	11.3	Choi et al. ³⁷
Al ₂ O ₃ Θ-phase	27Al	monoclinic	tetrahedral	80	79.5	Choi et al. ³⁷
BZY20	1H	cubic	Yttrium 1st & 2nd oxygen neighbor	5.4, 6.8	4.5, 6.8	Blanc et al. ³²
BZSc5	1H	cubic	Scandium 1st oxygen neighbor	4.4		Buannic et al. ³³
BZSc15	1H	cubic	Scandium 1st oxygen neighbor	4	3.7-4.9	Buannic et al. ³³
BZSc30	1H	cubic	Scandium 1st oxygen neighbor	3.3		Buannic et al. ³³
Sr ₃ LaNbO ₁₂	1H	hexagonal	1 Nb-O 3 Sr/La-O bonds, 2 Nb-O 2 Sr/La-O bonds	5, 3.4, 1.3		Tabacaru et al. ⁸
Ba ₂ In ₂ O ₄ (OH) ₂	1H	tetragonal	planar O-H-O, cross-plane O-H-O	7.3, 3.3, 1.7	8.5-9.7, 3.8 - 5.3	Dervisoglu et al. ³¹

the 4.0 ppm signal is best attributed to protons bonded to the O2 site lying in the BZO layer of

BIAZ³¹⁻³⁴. Protons from the 1.1 ppm and 0.7 ppm signals are attributed to protons at the sample surface due to their low concentration in manipulated samples, lack of spatial correlation to aluminum, and lack of evidence in literature as a bulk proton sites^{8,31-33}.

The proton signal around detected between 7.5-8.5 ppm had no observed correlation to aluminum or ¹H literature of doped BZO, making its proton signal most difficult to determine. Based upon its chemical shift, low concentration, and reports in literature, this signal is attributed to O5-O4 bonded protons, for the case of minority position indium in the oxygen deficient h' layer. Dervisoglu et al observed a chemical shift of 7.3 ppm, with a theoretically calculated chemical shift between 8.5-9.7, for protons bonded between planar O3 positions in the proton conductive hydrated Ba₂In₂O₄(OH)₂³¹. In their work, proton signals were also detected at 3.3 and 1.7 ppm, which were assigned to protons bonded between O1 and O2 positions within Ba₂In₂O₄(OH)₂³¹, as shown in

Table 8. The O1 and O2 positions form an indium polyhedral, with OH bonds crossing

Material	Nucleus of interest	Crystal structure	Configuration or Coordination	Observed chemical shift	Calculated chemical shift	Source
Ba ₂ In ₂ O ₄ (OH) ₂	17O	tetragonal	unprotonated oxygen, proton acceptor oxygen, proton donor oxygen	140, 174, 192, 207	197-223, 204-225, 169-185, 137-171	Dervisoglu et al. ³¹
BaZrO ₃	17O	Cubic	4 planar barium, 2 linear zirconium	376		Bastow et al. ³⁶
SrZrO ₃	17O	Orthorhombic	3 strontium, 2 zirconium	343/340		Bastow et al. ³⁶
CaZrO ₃	17O	Orthorhombic	3 calcium, 2 zirconium	336/329		Bastow et al. ³⁶
BaTiO ₃	17O	tetragonal	4 planar barium, 2 linear titanium	564/523		Bastow et al. ³⁶
SrTiO ₃	17O	Cubic	4 planar strontium, 2 linear titanium	465		Bastow et al. ³⁶
Al ₂ O ₃ Θ-phase	27Al	monoclinic	octahedral	10.5	11.3	Choi et al. ³⁷
Al ₂ O ₃ Θ-phase	27Al	monoclinic	tetrahedral	80	79.5	Choi et al. ³⁷
BZY20	1H	cubic	Yttrium 1st & 2nd oxygen neighbor	5.4, 6.8	4.5, 6.8	Blanc et al. ³²
BZSc5	1H	cubic	Scandium 1st oxygen neighbor	4.4		Buannic et al. ³³
BZSc15	1H	cubic	Scandium 1st oxygen neighbor	4	3.7-4.9	Buannic et al. ³³
BZSc30	1H	cubic	Scandium 1st oxygen neighbor	3.3		Buannic et al. ³³
Sr ₃ LaNbO ₁₂	1H	hexagonal	1 Nb-O 3 Sr/La-O bonds, 2 Nb-O 2 Sr/La-O bonds	5, 3.4, 1.3		Tabacaru et al. ⁸
Ba ₂ In ₂ O ₄ (OH) ₂	1H	tetragonal	planar O-H-O, cross-plane O-H-O	7.3, 3.3, 1.7	8.5-9.7, 3.8 - 5.3	Dervisoglu et al. ³¹

multiple ab planes³⁴. Compared to BIAZ, O5-H-O4 protons best resemble protons attributed to

high chemical shift signals in $\text{Ba}_2\text{In}_2\text{O}_4(\text{OH})_2$. This interpretation was achieved based upon the low concentration of the signal, the relatively variable but acidic chemical shift, and similarities to hydrated barium indium oxides^{31,34}.

With the knowledge neutron diffraction provides, there is much more confidence in the existence and structure of indium coordinating the h' layer. The O5 site must correlate to octahedral indium in the hexagonal layer, as previously discussed, and a proton signal coming from this region provides strong evidence of O5 protonation. This likely occurs via the same hydration process as O3, with water filling the vacant O4 site bringing two protons along in the process. In the case of majority or minority crystal structure, neutron diffraction indicates the O4 site is protonated, providing further evidence of hydrogen bonding to the O5 site.

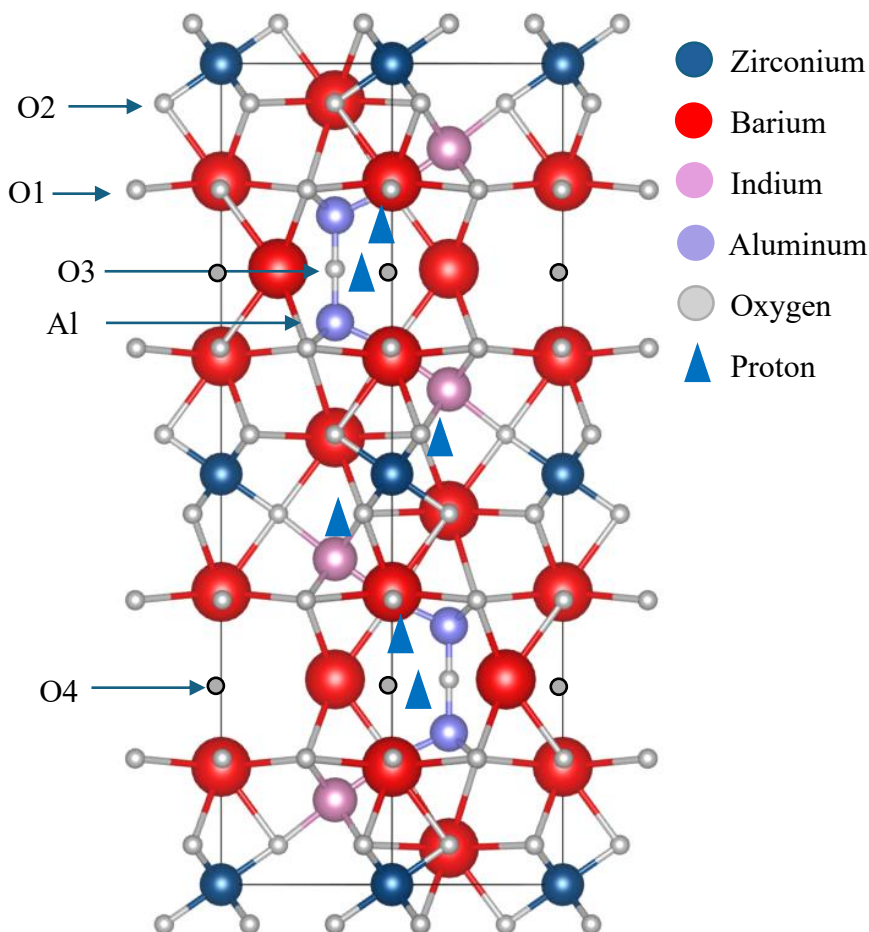


Figure 22. Crystal structure of BIAZ highlighting NMR investigated nuclear positions. Protons are shown at predicted sites identified via ^1H NMR, size and quantity of protons are not to scale. Model made using VESTA software.

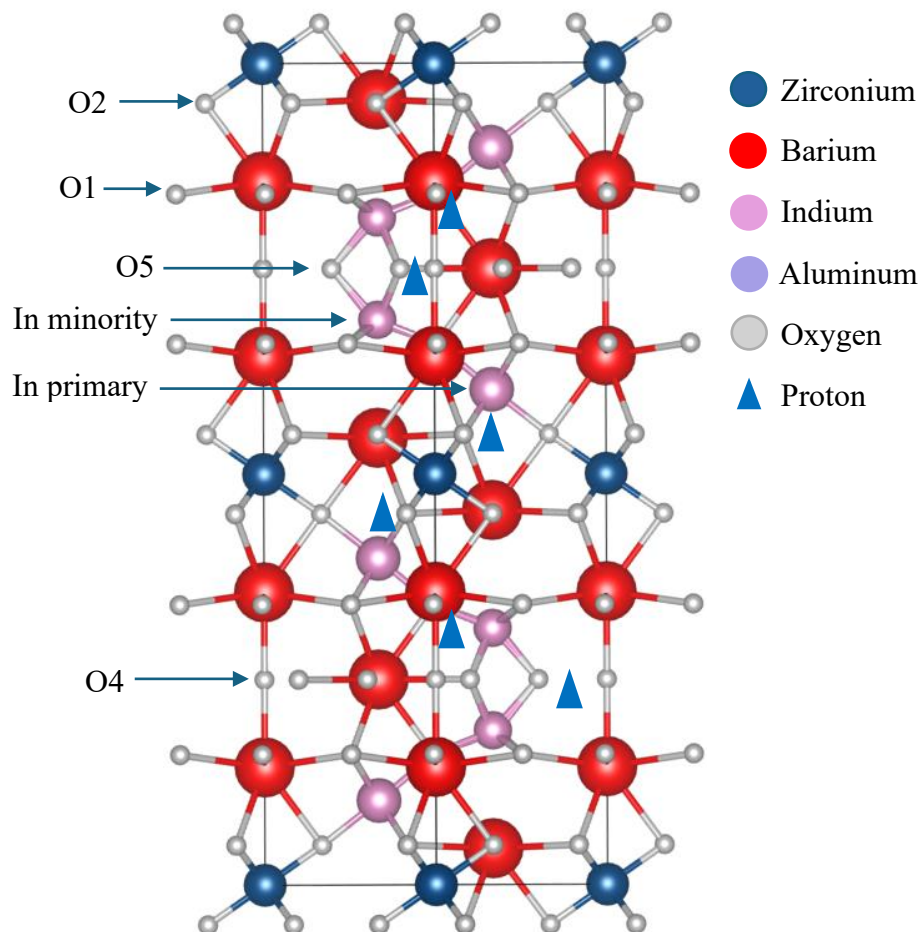


Figure 23. Minority crystal structure BIAZ, with O5 occupying the h' layer rather than O3. Protons are shown at predicted sites identified via ^1H NMR, size and quantity of protons are not to scale. Model made using VESTA software.

Placing assigned proton signals in the context of proton uptake and migration, our conclusions remain consistent. DFT calculations of BEAZ from Youn et al. observed thermodynamically favorable proton uptake at the O3/O4 site¹⁰. Incorporation of protons at the O4 and O2 sites was also thermodynamically favorable, although there was a slight increase in

the associated energy barrier¹⁰. This gave stronger evidence to support conclusions from Andreev et al., who proposed the BZO layer played a role in hydration of BIAZ based upon thermogravimetric analysis³⁵. DFT calculations determined the lowest energy barrier for proton migration was through the zirconate layer, with protons hopping along O2 sites. The theoretical discovery of anisotropic proton conduction along the ab plane was consistent with proton conduction data extrapolated from experimental data, measuring conduction of BEAZ thin films grown with preferentially oriented grains¹⁰.

When manipulating proton concentrations in BIAZ samples (hydration or ¹⁷O enrichment), the intensity of 5.1 and 4.0 ppm signals increases in hydrated samples and decreases in dehydrated samples. Given their attributed sites at favorable proton uptake positions, the signals would be expected to change due to hydration/dehydration.

Any sample preparation, hydration or dehydration, results in the largest proton signal existing at 1.8 ppm. Given its constant intensity in hydrated or dehydrated samples, there is an implication of proton trapping at this site, although the attributed O1 site has not previously been reported to exhibit proton trapping. DFT calculations by Youn et al. found that protons bonded to the O1 site, while hydrogen bonded to the O4 site, are in a local minima of thermodynamic stability¹⁰. There is a low energy barrier preventing migration of O3 - H - O4 to O1 - H - - - O4, and a very high energy barrier preventing further proton migration to the zirconate layer¹⁰. A proton site that can be easily reached, but not easily passed, would make sense for a signal with signs of proton trapping.

Material	Nucleus of interest	Crystal structure	Configuration or Coordination	Observed chemical shift	Calculated chemical shift	Source
Ba ₂ In ₂ O ₄ (OH) ₂	17O	tetragonal	unprotonated oxygen, proton acceptor oxygen, proton donor oxygen	140, 174, 192, 207	197-223, 204-225, 169-185, 137-171	Dervisoglu et al. ³¹
BaZrO ₃	17O	Cubic	4 planar barium, 2 linear zirconium	376		Bastow et al. ³⁶
SrZrO ₃	17O	Orthorhombic	3 strontium, 2 zirconium	343/340		Bastow et al. ³⁶
CaZrO ₃	17O	Orthorhombic	3 calcium, 2 zirconium	336/329		Bastow et al. ³⁶
BaTiO ₃	17O	tetragonal	4 planar barium, 2 linear titanium	564/523		Bastow et al. ³⁶
SrTiO ₃	17O	Cubic	4 planar strontium, 2 linear titanium	465		Bastow et al. ³⁶
Al ₂ O ₃ Θ-phase	27Al	monoclinic	octahedral	10.5	11.3	Choi et al. ³⁷
Al ₂ O ₃ Θ-phase	27Al	monoclinic	tetrahedral	80	79.5	Choi et al. ³⁷
BZY20	1H	cubic	Yttrium 1st & 2nd oxygen neighbor	5.4, 6.8	4.5, 6.8	Blanc et al. ³²
BZSc5	1H	cubic	Scandium 1st oxygen neighbor	4.4		Buannic et al. ³³
BZSc15	1H	cubic	Scandium 1st oxygen neighbor	4	3.7-4.9	Buannic et al. ³³
BZSc30	1H	cubic	Scandium 1st oxygen neighbor	3.3		Buannic et al. ³³
Sr ₃ LaNbO ₁₂	1H	hexagonal	1 Nb-O 3 Sr/La-O bonds, 2 Nb-O 2 Sr/La-O bonds	5, 3.4, 1.3		Tabacaru et al. ⁸
Ba ₂ In ₂ O ₄ (OH) ₂	1H	tetragonal	planar O-H-O, cross-plane O-H-O	7.3, 3.3, 1.7	8.5-9.7, 3.8 - 5.3	Dervisoglu et al. ³¹

Table 8. Previous literature analysis of NMR data obtained from similar materials

3.6.2 ^{27}Al NMR

With 98-100% of aluminum signal coming from 70 ppm chemical shift, it can be confidently stated aluminum nuclei in BIAZ hold a tetrahedral coordination^{16,37}. 1-2% of aluminum signal was detected below 10 ppm in non-hydrated samples, indicating rare positions of octahedral aluminum^{16,37}, although XRD analysis did not show any signs of impurity phases. Quadrupolar coupling constants indicate an asymmetric electric field gradient (EFG), whether from varying charges or varying bond length/angles of an atom's coordinating ions³⁸. In BIAZ, differences in Al-O3 and Al-O1 bond length/angles are expected to create an asymmetric EFG around aluminum nuclei^{6,38}. The slight reduction of quadrupolar coupling seen in hydrated samples implies an improved symmetry of the EFG, most likely caused by protonation of the O3 site.

The proven tetrahedral coordination of aluminum, along with neutron diffraction data, leads to the conclusion of aluminum only occupying its primary position (M2). In order for tetrahedral aluminum to maintain its tetrahedra at the indium position, there would need to be a unique oxygen site detected in the cubic layers. In addition to this, investigation of doped BZO, including Al³⁺ doped BZO, have provided strong evidence for the existence oxygen vacancies creating pentahedral coordination, but to the best of our knowledge none have predicted a tetrahedral coordination^{39,40}.

3.6.3 ^{17}O NMR

Of the eight oxygen signals discovered, only one was successfully attributed to an oxygen site in BIAZ. The 360 ppm signal was identified as the O2 site based upon its position in the zirconate layer. Previous studies of ABO_3 materials showed the ^{17}O chemical shift was strongly determined by the presence of zirconium, as shown in Table 8^{36,41}. BIAZ and similar hexagonal perovskites are known to contain four unique oxygen sites, making identification of all eight signals difficult. Given the five identified oxygen sites via neutron diffraction, the eight unique signals are likely result of indium site swapping along with protonated and unprotonated oxygens. In a less exciting perspective, it has been previously reported in various materials that multiple nuclear signals can be attributed to the same atomic site without having expected changes at the site^{8,31,36}.

CHAPTER 4. EIS ANALYSIS OF BIAZ

4.1 Preparation of EIS samples and experimental conditions

Pellets of BIAZ2.6, BIAZ2.8, BIAZ2.0 were prepared for EIS by applying conductive silver adhesive paste for electrodes. All pellets were above 92% dense, with BIAZ2.6 having a relative density above 98%. Tests were done in wet air and dry air. Wet air atmospheres had $p_{H_2O} = 0.0261$ atm, and dry atmospheres were controlled by passing air through Drierite before reaching the sample container. Humidity of the dry air atmosphere was not measured, but is assumed to be lower than the wet atmosphere by more than an order of magnitude. Samples were tested from 400°C to 650°C, an appropriate temperature range for intermediate temperature PCFCs, with a thermocouple used to monitor true sample temperature inside the contained atmosphere. In wet air an applied AC voltage of 80 mV was used, and for dry air an applied voltage of 100 mV was used. These values were determined by using the lowest voltage necessary to produce a meaningful NYQUIST plot. Tests in air were run from 5 MHz to 1 Hz, and tests in hydrogen were run from 5 MHz to 0.1 Hz.

4.2 Wet air EIS of BIAZ

Wet air BIAZ impedance data provided a Nyquist plot displaying a single semi circle from high to low frequencies, attributed to a combination of bulk and grain boundary behavior based upon capacitance values between 10^{-9} to 10^{-10} ⁴². Attempts to separate bulk and grain boundary components were unsuccessful, with no fittings able to detect a region with capacitance on the order of 10^{-12} , the expected capacitance for a bulk component ⁴². Bulk and grain boundary behavior were accordingly fitted to a resistor in series with a resistor and constant phase element (CPE) in parallel, as shown in Figure 24. A constant phase element is similar to a capacitor, but exhibits a frequency independent negative phase between current and

voltage⁴³. The use of resistor and CPE in parallel is consistent with equivalent circuits of other ionically conductive hexagonal perovskites^{9,11}. Conductivity values were extracted from the calculated bulk and grain resistance. BIAZ2.8 exhibited the highest conductivity and BIAZ2.6 exhibited the lowest conductivity, as shown in Figure 25. Conductivity values were on the expected order of magnitude for BIAZ¹¹, although the behavior of BIAZ2.6 was different with a constant activation energy across the entire temperature range.

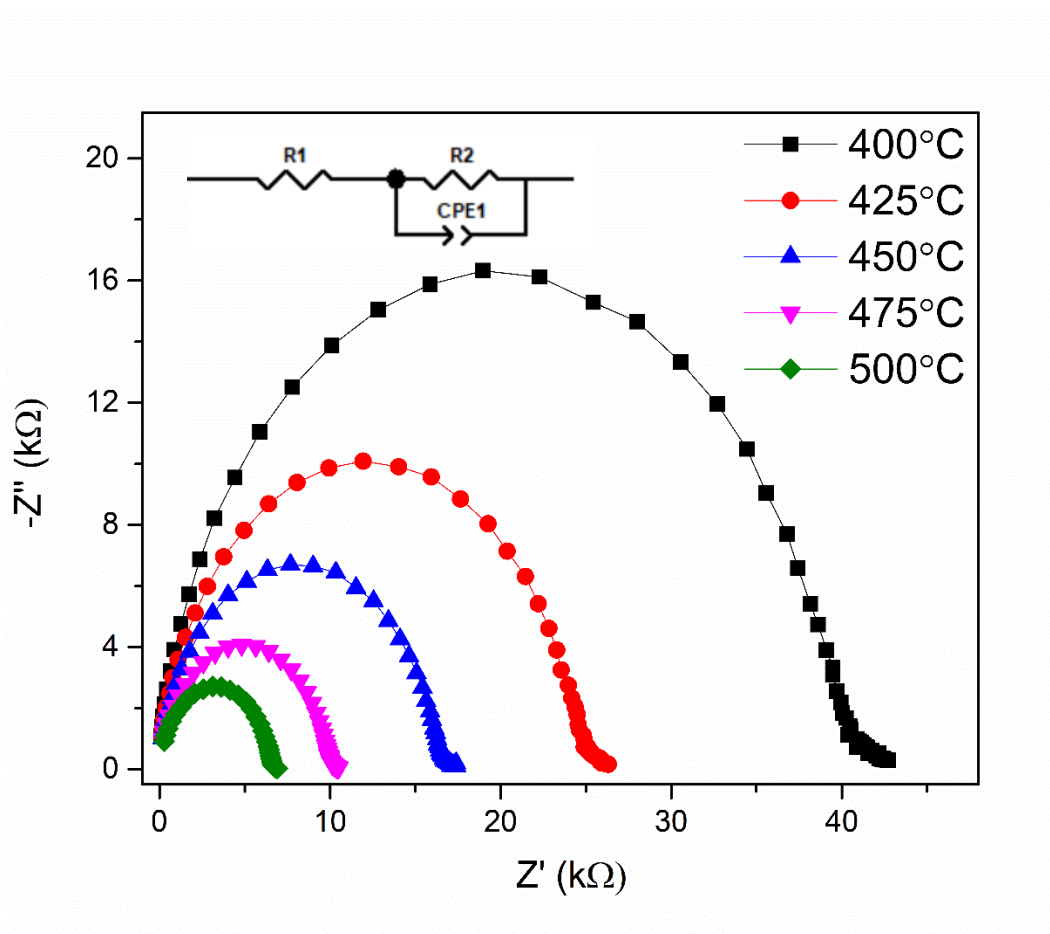


Figure 24. Nyquist plot of BIAZ2.6 from 400°C to 500°C in wet air conditions with associated equivalent circuit.

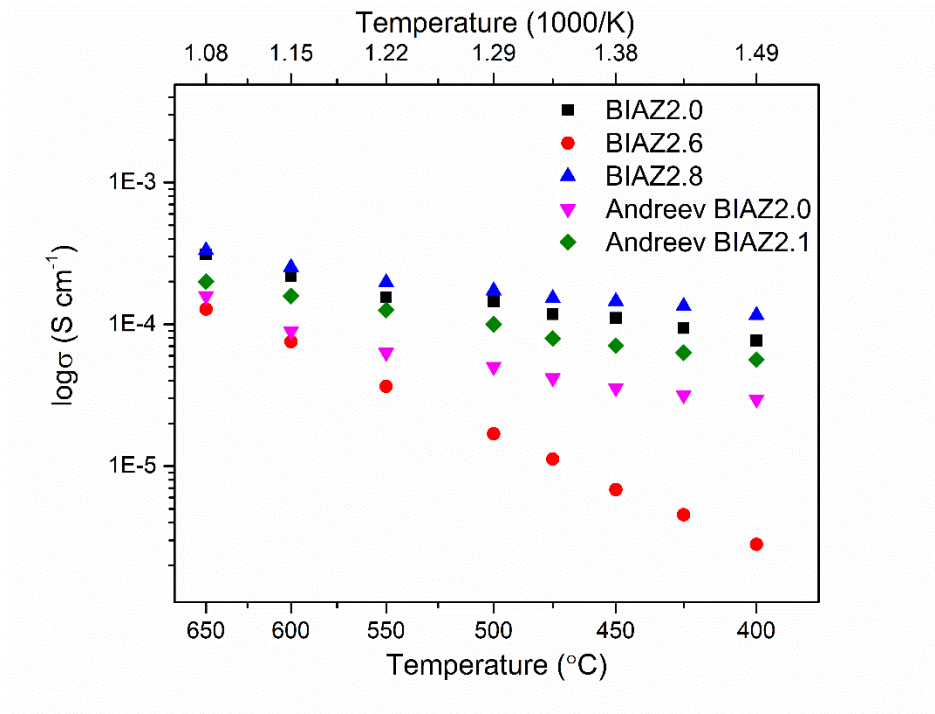


Figure 25. Conductivity trends of BIAZ in wet air conditions

4.3 Dry air EIS of BIAZ

Dry air BIAZ impedance data exhibited similar behavior to wet air BIAZ, with data best fit to the same equivalent circuit, as shown in Figure 26. BIAZ2.6 exhibited the highest conductivity above 500°C, but held the lowest conductivity at and below 500°C. There was an unexpected increase in conductivity between 500°C and 450°C for BIAZ2.0 and BIAZ2.8, which was not experienced by BIAZ2.6. All samples were tested at the same time and checked for stability at each temperature, removing the possibility of atmosphere/temperature changes impacting BIAZ2.8 and BIAZ2.0 results. BIAZ2.0 and BIAZ2.8 experienced a slight increase in activation energy beyond this point, while BIAZ2.6 again remained constant, as shown in Figure 27.

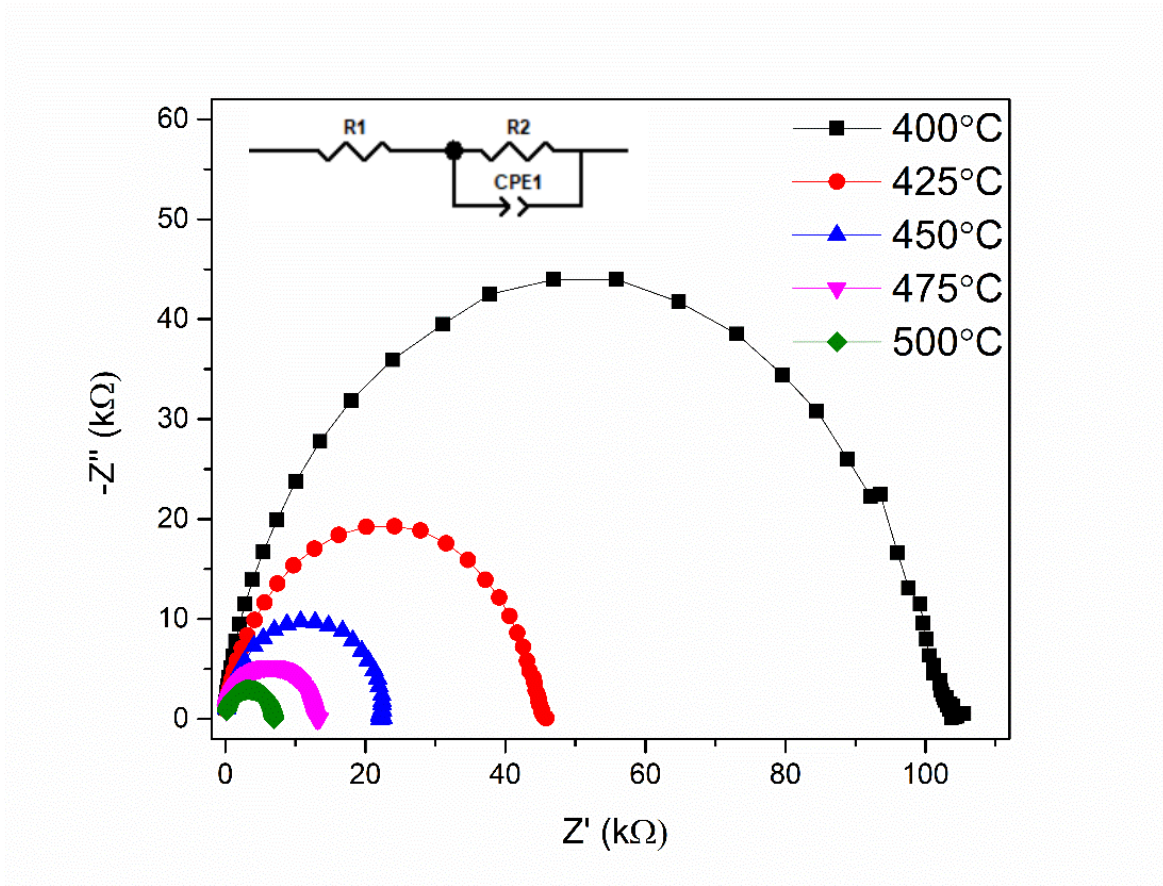


Figure 26. Nyquist plot of BIAZ2.6 in dry air conditions with associated equivalent circuit

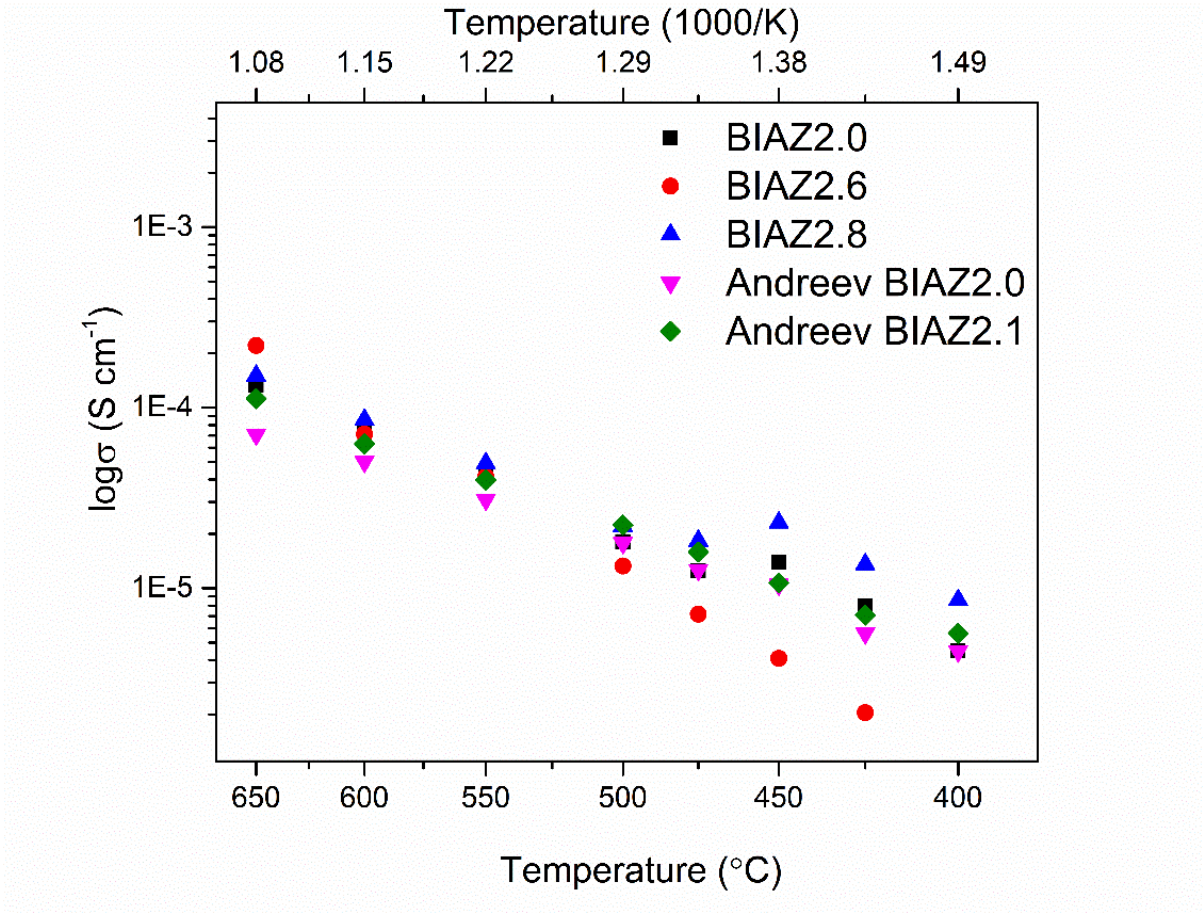


Figure 27. Conductivity trends of BIAZ in dry air conditions

4.6 Analysis of EIS results

4.6.1 Proton behavior in BIAZ

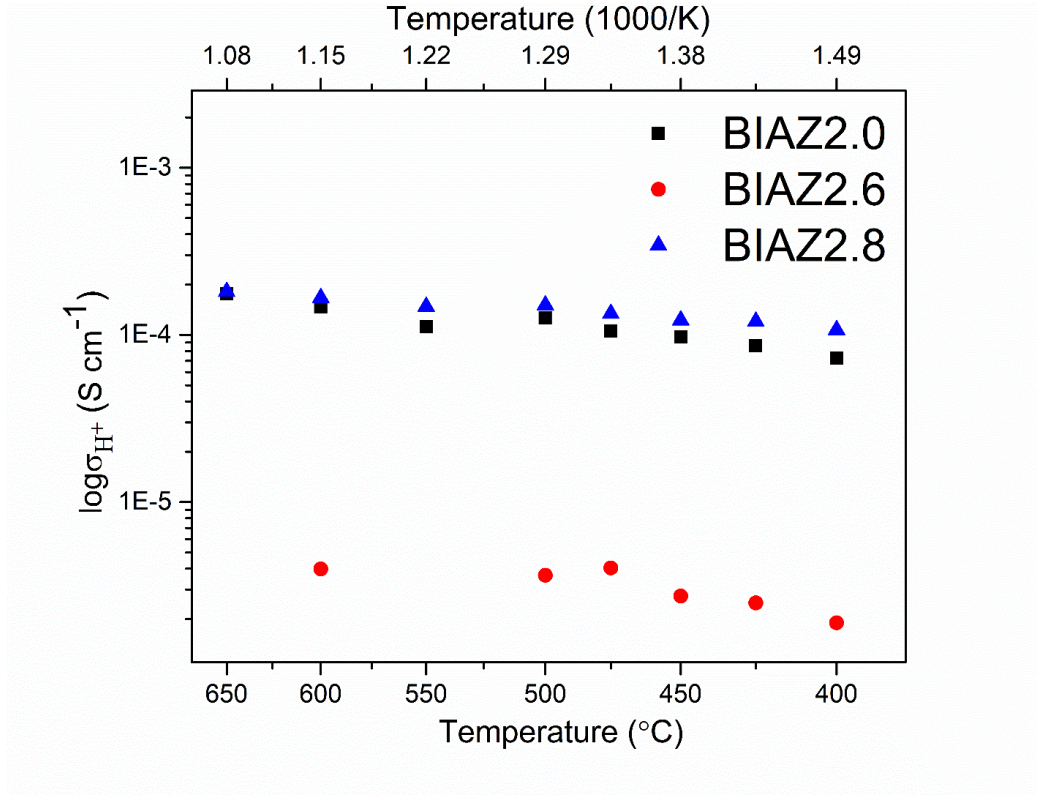


Figure 28. Estimated proton conductivity of BIAZ from wet and dry air conditions

$$\sigma_{\text{H}^+} = \sigma_{\text{wet air}} - \sigma_{\text{dry air}}$$

Equation 11. ^{5,11,26,44,45}

Proton conductivity plotted in Figure 28 was calculated from Equation 11. This approach has been the preferred method of calculating proton conductivity in layered hexagonal perovskites studied through EIS, which assumes the increase in conductivity from dry to wet conditions results from the humid atmosphere offering a proton supply to the material ^{5,11,26,44}.

Proton conductivity of BIAZ determined in previous literature was slightly lower than the BIAZ2.0 and BIAZ2.8 samples, but an order of magnitude higher than the BIAZ2.6 sample^{11,25}. The calculated proton unexpectedly low proton conductivity of BIAZ2.6 raised some concerns, which were not helped by the negative calculated proton conductivity at 650°C and 550°C. BIAZ2.6 was tested after BIAZ2.8 and BIAZ2.0 using the exact same conditions, but this creates the possibility of differing atmospheres. However, the decrease in activation energies between wet and dry air samples was consistent among all samples, reducing concerns of differing atmospheres between wet air experiments. Proton conductivity was very consistent across the tested temperature, which is seen in the low calculated activation energy of proton conduction.

Proton conductivity of BIAZ was lower than layered perovskites tested by Murakami et al., as expected, but still performed well compared to proton conducting layered perovskites of the form AA'BO₄^{5,45,46}. These layered perovskites, composed of perovskite layers divided by rock salt layers, exhibit a lower proton conductivity by over an order of magnitude than BIAZ above 600°C with the exception of BaNd_{0.9}Ca_{0.1}InO_{3.95} and BaNd_{0.8}Ca_{0.2}ScO_{3.95}⁴⁶.

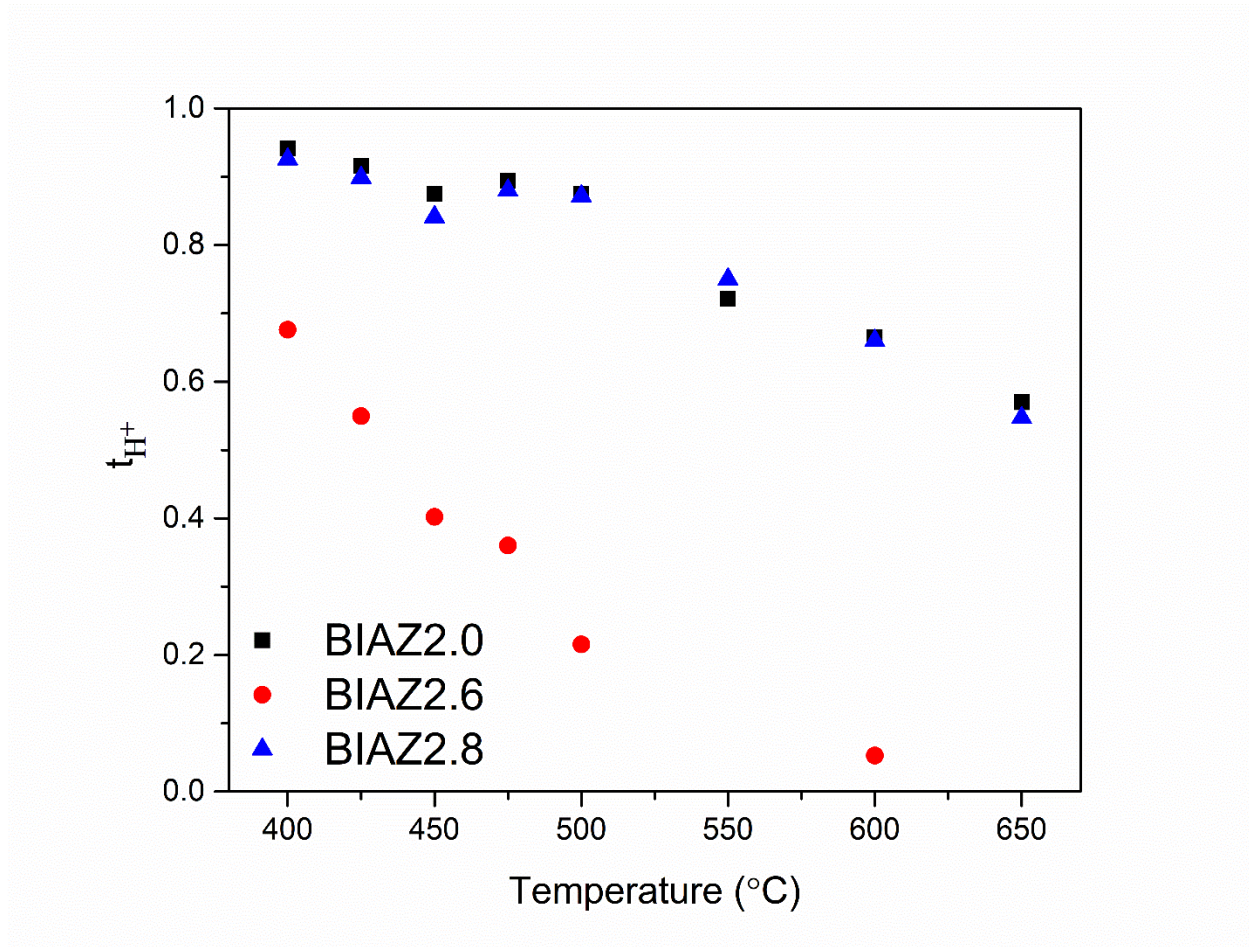


Figure 29. Estimated proton transport number of BIAZ from wet and dry air conditions

$$t_{H^+} = \frac{\sigma_{\text{wet air}} - \sigma_{\text{dry air}}}{\sigma_{\text{wet air}}}$$

Equation 12.

The proton transport number, calculated from the formula in Equation 12, represents the proportion of conduction in a material attributed to protons. Proton transport decreased with increasing temperature, which matched expected behavior based upon the results of Andreev et al.¹¹. With increasing temperature over the tested range, it becomes increasingly difficult to

hydrate the material. Andreev et al. observed no significant dehydration in BIAZ above 600°C, and Murakami et al. noted a decrease in wet conductivity from 450-800°C due to dehydration in BEAZ^{5,11}.

Although there were similar trends in transport numbers, the calculated transport numbers were different. Proton transport was previously reported to be approximately 0.7 at 500°C and approximately 0.4 at 650°C. BIAZ2.0 and BIAZ2.8 exhibited higher transport numbers, while BIAZ2.6 exhibited significantly lower transport numbers. At the points 550°C and 650°C, the transport numbers are not visible as they were calculated to negative values. Again, this poses questions for the true atmospheric conditions of the wet air BIAZ2.6 experiment.

4.6.2 Activation energy of BIAZ

The activation energies of BIAZ are displayed in tables 9 and 10, calculated from equation 10 showed in section 1.2.5. By plotting the temperature on a 1000/K scale and the conductivity on a log scale, the Arrhenius equation is used to determine activation energies²⁴. Activation energies were higher in dry air environments than wet air environments, which was to expected from a proton conductor^{5,25}. Surprisingly, the activation energy of conduction in wet air decreased at lower temperatures, which was not seen in previous literature of BIAZ²⁵. This was further confirmed by a slight decrease in the activation energy of proton conduction at lower temperatures for BIAZ2.0 and BIAZ2.8.

Compared to previous literature of BIAZ, samples BIAZ2.0 and BIAZ2.8 tested in this work exhibited lower activation energies for wet air, dry air, and the calculated proton conductivity. Previous literature of BIAZ2.0 determined a dry air activation energy of 0.67 eV

and wet air activation energy of 0.33 in wet air from 250-500°C¹¹. Andreev et al. also determined the activation energy of proton conduction in BIAZ2.0 was calculated to be 0.27 eV below 450°C²⁵. Samples tested in the work from Andreev et al. exhibited activation energies in wet air comparable to the analogous compositions investigated by Murakami et al.^{5,11,25}. BIAZ2.6, despite having lower conductivities than BIAZ2.0, BIAZ2.8, and samples tested by Andreev et al., had calculated activation energies much closer to expected values in BIAZ^{5,25}.

The temperature range of experiments in this work was much smaller than previous studies of BIAZ, with the low end activation energies calculated from 400°C to 450°C and high end activation energies from 550°C to 650°C, compared to 250-500°C and 700-900°C²⁵. This discrepancy is a possible reason for the differences in trends of activation energies. In addition, an analysis of proton conductivity versus hole conductivity was not done. Previous BIAZ studies investigated hole conduction by analyzing conduction behavior in the context of varied oxygen partial pressures.

Table 9. Activation energies of BIAZ from 550°C to 650°C

	BIAZ2.0	BIAZ2.6	BIAZ2.8
Wet	0.2 eV	0.36 eV	0.15 eV
Dry	0.32 eV	0.48 eV	0.32 eV
Proton	0.13 eV	0.02 eV	0.06 eV

Table 10. Activation energies of BIAZ from 400°C to 450°C

	BIAZ2.0	BIAZ2.6	BIAZ2.8
Wet	0.13 eV	0.32 eV	0.08 eV
Dry	0.41 eV	0.55 eV	0.36 eV
Proton	0.11 eV	0.05 eV	0.05 eV

4.6.3 BIAZ conductivity in context

When investigating the proton conductivity of BIAZ in context, a correlation is observed between decreasing *ab* lattice constant and increasing conductivity. The trend is consistent within this work, however other factors are assumed to impact proton conductivity. The experiments run by Andreev et al. were on samples with significantly larger *ab* lattice constants than those from this work (see Table 2), however their conductivity values are approximately the same¹¹. The samples tested by Andreev et al. were not produced using the same synthesis approach and based upon XRD results were not 100% phase pure, increasing the difficulty of direct comparisons.

Compared with hexagonal perovskites investigated by Murakami et al., BIAZ exhibits an order of magnitude lower conductivity in wet conditions⁵. Given proton conduction is theorized to occur through the zirconate layer, the cubic layers of Ba₅M₂Al₂ZrO₁₃ were compared. In previous studies of doped BZO, doping with trivalent cations that are more easily incorporated into the lattice was correlated to lower proton conductivity. This was proven by Giannici et al. who compared In³⁺, Y³⁺, and Gd³⁺ doped BZO, observing lower solubility and higher proton conductivity with larger dopants⁴⁰. They determined the lattice disorder caused by larger cations, being more difficult to incorporate, created a more localized trivalent defect. Giannici et al. related this localized defect to improved proton conductivity. Contrarily, the lack of disorder near

easily incorporated cations like In^{3+} would spread excess negative charge, impacting oxygen basicity and O-H bonding⁴⁰. The rare earth dopants investigated by Murakami et al. have ionic radii larger than In^{3+} and closer to the Y^{3+} and Gd^{3+} cations studied by Giannici et al.^{5,40,47}.

Another factor contributing to the calculated proton conductivity is the level of hydration in the samples. In comparison with BEAZ, Youn et al. measured hydration times for samples of different sizes, with complete hydration of the 1 mm thickness sample taking over 100 hours at 600°C. In our testing, it was not possible to provide 100+ hours for hydration due to time constraints on equipment use¹⁰. Measurements were always tested for consistency before moving on to the next temperature step, however this hydration time could have played an impact. Murakami et al. showed stable hydration in their samples after 30-40 hours, the time frame used in this work, with samples of lower relative density^{5,11,25,35}. Previous literature of BIAZ does not specify the time provided for hydration^{11,25,35}.

CHAPTER 5. CONCLUSIONS AND FUTURE WORK

5.1 Chemistry and structure of BIAZ

This work showed BIAZ was capable of incorporating higher indium contents than previously reported, with the highest calculated In/Zr ratio reaching 2.85. Site swapping between indium and aluminum was shown to be one way, with indium occupying the M1 site approximately 80% of the time and the M2 site approximately 20% of the time, while aluminum only occupies the M2 position. Indium holds an octahedral coordination at both positions, inducing the formation of O5 sites in the h' layer when in the minority M2 site, while aluminum holds a strictly tetrahedral coordination. Statistical site swapping did not change between samples of different projected indium content, implying a substitution of In^{3+} for Zr^{4+} and theoretically inducing an increase in the oxygen vacancy concentration, although ICPMS results did not indicate oxygen deficiencies. Increasing the indium content was observed to correlate with a decrease in the c lattice constant, which was not assumed to play a role in conductivity values due to preferential conduction along the ab plane.

Proton NMR indicated the existence of four proton sites within BIAZ, three of which heavily influenced by hydration of the material. Based upon the chemical shifts of these signals, protons appear to bond to O2 in the zirconate layer, between O3 and O4 in the h' layer when aluminum occupies the M2 site, and between O5 and O4 in the h' layer when indium occupies the M2 site. These signals account for approximately 25% of protons detected in hydrated BIAZ, with the remaining 75% best attributed to O1 protons, implying a proton trapping mechanism between the hexagonal and cubic layers of BIAZ. Oxygen NMR detected eight oxygen signals, only one of which could be confidently identified as the O2 site. The remaining oxygen signals are likely the result of protonated and unprotonated oxygens throughout the lattice.

5.2 Conductivity of BIAZ

BIAZ in wet air exhibited total conductivity on the order of 10^{-4} S cm^{-1} from 400-650°C, while dry conductivity was above 10^{-5} from 500-650°C and above 10^{-6} S cm^{-1} below 500°C. Bulk and grain boundary conductivities were measured as one, given the lack of evidence for a bulk component in the impedance data. Proton conductivity was shown to have a very low lower activation energy in the tested temperature range compared with literature, and proton transport decreased with increasing temperature. Due to these patterns, at low temperatures conductivity is assumed to be dominated by protons, with increasing contribution from dominated by oxygen ions and hole conduction at higher temperatures. A correlation between decreasing ab lattice parameter and increasing proton conductivity was observed, with some concerns to the validity of the BIAZ2.6 measurements due to an order of magnitude difference from other samples' proton conductivities.

5.3 Future Work

Variable temperature ^1H NMR of BIAZ would yield stronger conclusions to the locations of proton signals detected. Observing the changes in the shape, intensity, and chemical shifts of the signals provides useful information on proton behavior that can't be observed when studying room temperature samples. DFT calculations of oxygen NMR would provide a better understanding of the oxygen signals detected, adding more evidence to the protonated and unprotonated oxygen sites and their relative concentrations.

Testing samples in a 5% H_2 atmosphere will provide insight to the behavior of BIAZ when exposed to a reducing atmosphere, which is important when characterizing a material for PCFC

electrolyte applications. Testing the samples in wet and dry hydrogen atmospheres will further improve the understanding of proton behavior in BIAZ.

SEM and EDX of BIAZ samples would allow for understanding of the microstructure and homogeneity of elements in samples. This information could provide important clarification to the analysis of BIAZ conductivity, given the anisotropic nature of proton conduction in these layered perovskites. The knowledge of grain sizes and orientations would allow for more complete conclusions on conductivity's dependence with indium concentration and ab lattice parameters.

Calorimetry of BIAZ would investigate its thermochemical properties, looking into the enthalpy of formation and associated energy barriers for chemical reactions within the structure. This knowledge would improve the fundamental understanding of the material's stability and performance as a proton conducting electrolyte.

REFERENCES

1. Carrette, L., Friedrich, K. A. & Stimming, U. Fuel Cells: Principles, Types, Fuels, and Applications. *ChemPhysChem* **1**, 162–193 (2000).
2. Ormerod, R. M. Solid oxide fuel cells. *Chemical Society Reviews* vol. 32 17–28 Preprint at <https://doi.org/10.1039/b105764m> (2003).
3. Cao, J., Ji, Y. & Shao, Z. Perovskites for protonic ceramic fuel cells: a review. *Energy and Environmental Science* vol. 15 2200–2232 Preprint at <https://doi.org/10.1039/d2ee00132b> (2022).
4. Dunn, B., Kamath, H. & Tarascon, J. M. Electrical energy storage for the grid: A battery of choices. *Science* vol. 334 928–935 Preprint at <https://doi.org/10.1126/science.1212741> (2011).
5. Murakami, T., Hester, J. R. & Yashima, M. High Proton Conductivity in Ba₅Er₂Al₂ZrO₁₃, a Hexagonal Perovskite-Related Oxide with Intrinsically Oxygen-Deficient Layers. *J Am Chem Soc* **142**, 11653–11657 (2020).
6. Shpanchenko, R. V., Abakumov, A. M., Antipov, E. V & Kovba, L. M. Crystal Structure of Ba₅In₂Al₂ZrO₁₃. *Journal of Alloys and Compounds* vol. 206 (1994).
7. Shpanchenko, R. V., Abakumov, A. M. & Antipov, E. V. Structural Study of the New Complex Oxides Ba_{5-y}Sr_yR_{2-x}Al₂Zr_{1+x}O_{13+x/2} (R = Gd-Lu, Y, Sc). *J Solid State Chem* **118**, 180–192 (1995).
8. Tabacaru, C. *et al.* Protonic and electronic defects in the 12R-type hexagonal perovskite Sr₃LaNb₃O₁₂. *Solid State Ion* **253**, 239–246 (2013).
9. Fop, S. *et al.* High oxide ion and proton conductivity in a disordered hexagonal perovskite. *Nat Mater* **19**, 752–757 (2020).
10. Youn, Y. *et al.* Anisotropic Proton Migration in Hexagonal Perovskite-Related Ba₅Er₂Al₂ZrO₁₃ Oxide. *Chemistry of Materials* **35**, 9493–9504 (2023).
11. Andreev, R., Korona, D., Anokhina, I. & Animitsa, I. Proton and Oxygen-Ion Conductivities of Hexagonal Perovskite Ba₅In₂Al₂ZrO₁₃. *Materials* **15**, (2022).
12. Reif, B., Ashbrook, S. E., Emsley, L. & Hong, M. Solid-state NMR spectroscopy. *Nature Reviews Methods Primers* vol. 1 Preprint at <https://doi.org/10.1038/s43586-020-00002-1> (2021).
13. J. Keeler. *Understanding NMR Spectroscopy*. (University of Cambridge, 2002).
14. Laws, D. D., Bitter, H.-M. L. & Jerschow, A. Solid-State NMR Spectroscopy. *Angewandte Chemie International Edition* **41**, 2096–3129 (2002).

15. Kumari, B., Brodrecht, M., Gutmann, T., Breitzke, H. & Buntkowsky, G. Efficient Referencing of FSLG CPMAS HETCOR Spectra Using 2D 1H–1H MAS FSLG. *Appl Magn Reson* **50**, 1399–1407 (2019).
16. Walkley, B. & Provis, J. L. Solid-state nuclear magnetic resonance spectroscopy of cements. *Materials Today Advances* vol. 1 Preprint at <https://doi.org/10.1016/j.mtadv.2019.100007> (2019).
17. Abraham, A., Prins, R., van Bokhoven, J. A., van Eck, E. R. H. & Kentgens, A. P. M. TRAPDOR double-resonance and high-resolution MAS NMR for structural and template studies in zeolite ZSM-5. *Solid State Nucl Magn Reson* **35**, 61–66 (2009).
18. Medek, A. & Frydman, L. Multiple-Quantum Magic-Angle Spinning NMR: A New Technique for Probing Quadrupolar Nuclei in Solids. *Sociedade Brasileira de Química* **10**, 263–277 (1999).
19. Kanellopoulos, J., Freude, D. & Kentgens, A. A practical comparison of MQMAS techniques. *Solid State Nucl Magn Reson* **32**, 99–108 (2007).
20. Rocha, J., Morais, C. M. & Fernandez, C. Progress in Multiple-Quantum Magic-Angle Spinning NMR Spectroscopy. *Top Curr Chem* **246**, 141–194 (2005).
21. Laschuk, N. O., Easton, E. B. & Zenkina, O. V. Reducing the resistance for the use of electrochemical impedance spectroscopy analysis in materials chemistry. *RSC Advances* vol. 11 27925–27936 Preprint at <https://doi.org/10.1039/d1ra03785d> (2021).
22. Li, C. Gallium Substitution in Zirconate-Based Fast Ionic Conducting Ceramics. (Clemson University, 2016).
23. Han, P. ju, Zhang, Y. feng, Chen, F. Y. & Bai, X. hong. Interpretation of electrochemical impedance spectroscopy (EIS) circuit model for soils. *J Cent South Univ* **22**, 4318–4328 (2015).
24. Heins, T. P., Harms, N., Schramm, L. S. & Schröder, U. Development of a new Electrochemical Impedance Spectroscopy Approach for Monitoring the Solid Electrolyte Interphase Formation. *Energy Technology* **4**, 1509–1513 (2016).
25. Andreev, R. D., Anokhina, I. A., Korona, D. V., Gilev, A. R. & Animitsa, I. E. Transport Properties of In³⁺- and Y³⁺-Doped Hexagonal Perovskite Ba₅In₂Al₂ZrO₁₃. *Russian Journal of Electrochemistry* **59**, 190–203 (2023).
26. Andreev, R. D., Korona, D. V., Anokhina, I. A. & Animitsa, I. E. Novel Nb⁵⁺-doped hexagonal perovskite Ba₅In₂Al₂ZrO₁₃ (structure, hydration, electrical conductivity). *Chimica Techno Acta* **9**, (2022).
27. Rosman, K. J. R. & Taylor, P. D. P. ISOTOPIC COMPOSITIONS OF THE ELEMENTS 1997 (Technical Report). *Pure & Appl. Chern* **70**, 217–235 (1998).

28. Richard A. Tomasi. *A Spectrum of Spectral Problems*. (Sunbelt R & T, Incorporated, 1994).
29. d'Espinose de Lacaillerie, J. B., Fretigny, C. & Massiot, D. MAS NMR spectra of quadrupolar nuclei in disordered solids: The Czjzek model. *Journal of Magnetic Resonance* **192**, 244–251 (2008).
30. Stebbins, J. F., Zhao, P., Lee, S. K. & Oglesby, J. V. Direct observation of multiple oxygen sites in oxide glasses: recent advances from triple-quantum magic-angle spinning nuclear magnetic resonance. *Journal of non-crystalline solids* vols 293–295 67–83 Preprint at www.elsevier.com/locate/jnoncrysol (2001).
31. Dervişoğlu, R. *et al.* Joint Experimental and Computational ^{17}O and ^1H Solid State NMR Study of $\text{Ba}_2\text{In}_2\text{O}_4(\text{OH})_2$ Structure and Dynamics. *Chemistry of Materials* **27**, 3861–3873 (2015).
32. Blanc, F. *et al.* Dynamic nuclear polarization NMR of low- γ nuclei: Structural insights into hydrated yttrium-doped BaZrO_3 . *Journal of Physical Chemistry Letters* **5**, 2431–2436 (2014).
33. Buannic, L., Sperrin, L., Dervişoğlu, R., Blanc, F. & Grey, C. P. Proton distribution in Sc-doped BaZrO_3 : A solid state NMR and first principle calculations analysis. *Physical Chemistry Chemical Physics* **20**, 4317–4328 (2018).
34. List of Authors, C. *et al.* Short-Range Structure of the Brownmillerite-Type Oxide $\text{Ba}_2\text{In}_2\text{O}_5$ and its Hydrated Proton-Conducting Form BaInO_3H Short-Range Structure of the Brownmillerite-Type Oxide $\text{Ba}_2\text{In}_2\text{O}_5$ and its Hydrated Proton-Conducting Form BaInO_3H . *J Mater Chem A Mater* 1–12 (2014).
35. Andreev, R. & Animitsa, I. Transport Properties of Intergrowth Structures $\text{Ba}_5\text{In}_2\text{Al}_2\text{ZrO}_{13}$ and $\text{Ba}_7\text{In}_6\text{Al}_2\text{O}_{19}$. *Applied Sciences (Switzerland)* **13**, (2023).
36. Bastow, T. J. *et al.* Factors Controlling the ^{17}O NMR Chemical Shift in Ionic Mixed Metal Oxides A wide range of ^{17}O -enriched phases ABO. *Journal of Physical Chemistry* **100**, 18539–18545 (1996).
37. Choi, M., Matsunaga, K., Oba, F. & Tanaka, I. Al NMR chemical shifts in oxide crystals: a first-principles study. *Journal of Physical Chemistry C* **113**, 3869–3873 (2009).
38. Choh, S. H. *et al.* Calculation of electric field gradient tensor for simple point charge distributions and its application to real systems. *Journal of the Korean Magnetic Resonance Society* **7**, 16–24 (2003).
39. Gomez, M. A. *et al.* Oxygen vacancies altering the trapping in the proton conduction landscape of doped barium zirconate. *Journal of Physical Chemistry C* **124**, 27954–27964 (2020).

40. Giannici, F., Longo, A., Kreuer, K. D., Balerna, A. & Martorana, A. Dopants and defects: Local structure and dynamics in barium cerates and zirconates. *Solid State Ion* **181**, 122–125 (2010).
41. Bastow, T. J. & Stuart, S. N. *170 NMR IN SIMPLE OXIDES. Chemical Physics* vol. 143 (1990).
42. Irvine, J. T. S., Sinclair, D. C. & West, A. R. Electroceramics: Characterization by Impedance Spectroscopy. *Advanced Materials* **2**, 132–138 (1990).
43. Holm, S., Holm, T. & Martinsen, Ø. G. Simple circuit equivalents for the constant phase element. *PLoS One* **16**, (2021).
44. Ullah, A. *et al.* A multicomponent equimolar proton-conducting quadruple hexagonal perovskite-related oxide system. *Dalton Transactions* **52**, 1885–1894 (2023).
45. Morikawa, R. *et al.* High proton conduction in Ba₂LuAlO₅ with highly oxygen-deficient layers. *Commun Mater* **4**, (2023).
46. Tarasova, N. A., Animitsa, I. E., Galisheva, A. O. & Medvedev, D. A. Layered and hexagonal perovskites as novel classes of proton-conducting solid electrolytes. A focus review. *Electrochemical Materials and Technologies* **1**, 20221004 (2022).
47. Shannon, R. D. Revised Effective Ionic Radii and Systematic Studies of Interatomic Distances in Halides and Chalcogenides. *Acta Cryst* **32A**, 751–767 (1976).